Highly CO 2 -supersaturated melts in the Pannonian lithospheric mantle – A transient carbon reservoir?

Laura Créon, Virgile Rouchon, Souhail Youssef, Elisabeth Rosenberg, Guillaume Delpech, Csaba Szabo, Laurent Remusat, Smaïl Mostefaoui, Paul D Asimow, Paula M Antoshechkina, et al.

Highly CO_2-supersaturated melts in the Pannonian lithospheric mantle – A transient carbon reservoir?

Laura Créon [a], Virgile Rouchon [a], Souhail Youssef [a], Elisabeth Rosenberg [a], Guillaume Delpech [b], Csaba Szabó[c], Laurent Remusat [d], Smail Mostefaoui [d], Paul D. Asimow [e], Paula M. Antoshechkina [e], Mark S. Ghiorso [f], Elodie Boller [g] , François Guyot [d]

[a] IFP Energies nouvelles, 1 & 4 avenue Bois Préau, 92852 Rueil-Malmaison Cedex, France ; [b] Geosciences Paris Sud department, Paris Sud University, Bâtiment 504, 91405 Orsay Cedex, France ; [c] Lithosphere Fluid Research Lab, Department of Petrology and Geochemistry, Eotvos University, Pazmany Peter setany 1/c, H-1117 Budapest, Hungary; ;[d] IMPMC, Museum National d'histoire Naturelle, Sorbonne Universités, CNRS, UPMC, IRD, 61 Rue Buffon, 75005 Paris, France ; [e]California Institute of Technology, 1200 East California Blvd. Pasadena, California 91125, USA; [f]OFM Research, 7336 24th Avenue NE, Seattle, WA 98115 USA Seattle, Washington-USA; [g]ESRF, 71 Avenue des Martyrs, 38000 Grenoble, France

Corresponding Author: Laura Créon, lauracreon@gmail.com; Present address: Universidad Nacional Autónoma de México, Centro de Geociencias, Campus Juriquilla, A.P. 1-742, Boulevard Juriquila No. 3001, Juriquilla. Qro., C.P. 76230

Abstract

The carbon budget of the continental lithospheric mantle is poorly known, although it is believed to be substantially fed by subduction zones and a source of the widespread non volcanic CO_2 degassing occurring in active tectonic intracontinental settings. We propose new constraints on the CO_2 budget of the subcontinental lithospheric mantle below the Pannonian

Basin (Central Europe) through present study of a suite of xenoliths from the Bakony-Balaton Highland Volcanic Field. Trails of secondary fluid inclusions, silicate melt inclusions, network of melt veins and melt pockets with large and abundant vesicles, are numerous evidences of mantle metasomatism that affected the lithosphere beneath region. A quantitative estimate of the CO_2 budget of the mantle below the Pannonian Basin was constrained by an innovative approach applied to mantle xenoliths using (1) synchrotron X-ray microtomography, (2) NanoSIMS, Raman spectroscopy and microthermometry, and (3) thermodynamic models (Rhyolite-MELTS). The reconstructed 3D volumes obtained by synchrotron X-ray microtomography allow quantifying the proportions of all petrographic phases in the samples and to visualize their textural relationships. The concentrations of CO_2 and H_2O in glass veins and pockets range between 0.27 ± 0.01 (1σ) and 0.96 ± 0.02 (1σ), and 0.54 ± 0.26 (1σ) and 4.25 ± 0.27 (1σ) wt. %, respectively, and have higher CO_2 contents than typical arc magmas (0-0.25 wt. % CO_2 and 1.9-6.3 wt. % H_2O). Trapping vesicle pressures were determined based on silicate melt saturation pressures between 0.69 to 1.78 GPa, and are generally in excess compared to fluid inclusions trapping pressures determined by Raman spectroscopy and microthermometry (0.1-1.1 GPa). The CO_2/silicate melt mass ratios in the metasomatic agent that percolated the lithospheric mantle below the Pannonian Basin are estimated between 9.0 and 25.4 wt. %, indicating that silicate melts were CO_2 supersaturated in their source region. We suggest that slab derived melts initially containing up to 25 wt. % of CO_2 migrated congruently into the lithospheric mantle, and were subsequently fractionated by CO_2 segregation in secondary fluid inclusions by fracturing and creeping of the peridotite mineral matrix. A first order estimation of the bulk minimal CO_2 concentration in the lithospheric mantle below the Pannonian Basin is proposed at 1935 ppm. This transient carbon reservoir is believed to be degassed through the Pannonian Basin due to volcanism and

tectonic events, likely drained by the Mid-Hungarian Zone, a regional shear zone of lithospheric scale.

Keywords: X-ray microtomography; Mantle-xenoliths; CO_2-budget; Lithospheric-mantle

1 Introduction

The mantle is thought to be largest carbon reservoir of the Earth (Sleep et al., 2001; Shcheka et al., 2006; Dasgupta and Hirschmann, 2010; Dasgupta, 2013), containing more than 90% of carbon of the Earth (Poinar, 2012). Many geological processes depend on and attest for the existence of deep carbon and its exchange with other major terrestrial reservoirs, such as CO_2 degassing at mid-ocean ridges, CO_2-rich magmatism rooted in the mantle (kimberlites, carbonatites), and diamond or carbonate-bearing xenoliths originating from the deep mantle (Hammouda 2003 and references therein). In order to balance the continuous CO_2 degassing at volcanic centers, carbon must have been recycled into the mantle over geological time scales, most likely at convergent margins where carbonate-altered, sediment-bearing oceanic crust returns into the mantle (Zhang & Zindler 1993). Carbon dioxide is known to be a dominant volatile species in magmatic fluids and gases in subduction zone environments (Anderson, 1975; Fyfe et al., 1978) and its mantle origin has clearly been shown by $^{3}He/^{4}He$ and $\delta^{13}C$ isotopic ratios of fumaroles and hot spring gases (e.g. Sano & Marty, 1995). There have been several recent reviews of the carbon cycle in subduction environments (Jarrard, 2003; Wallace, 2005; Gorman et al., 2006; Dasgupta and Hirschmann, 2010; Johnston et al., 2011; Dasgupta, 2013; Burton et al., 2013), which estimate that about half of the subducted carbon is removed from the subducting plate beneath fore-arcs and arcs and returns surface of Earth [40% in Gorman et al. (2006); 20–80% in Dasgupta & Hirschmann (2010); and 18–70%

in Johnston et al. (2011)]. A large part of the subducted CO_2 is therefore thought to be stored in the mantle (Kelemen and Manning, 2015). Kelemen and Manning (2015) recently argued that the carbon input from subduction zones into the overlying plate is larger than output from arc volcanoes plus diffuse venting, and that substantial quantities of carbon are stored in the mantle lithosphere and crust. This recent study suggests that diffuse escape of CO_2 towards the surface and, more importantly, transient storage of CO_2 in the back-arc lithospheric mantle may, when added to the more commonly described fluxes of arc magma and MOR degassing, fully balance the subducted carbon (Kelemen and Manning, 2015). Therefore, both the diffuse degassing flux in back-arc regions and the lithosphere mantle carbon reservoir need to be further quantified since they have considerable implications for the global carbon cycle.

This study aims at constraining the magmatic CO_2 budget of the subcontinental lithospheric mantle below the Pannonian Basin (PB, Central Europe) through the study of a suite of petrographically and geochemically well-studied peridotite xenoliths (Creon et al., this volume) from the Balaton-Bakony Highland Volcanic Field (BBHVF, Szabó et al. 2010). The PB is known for its substantial mantle derived CO_2 accumulations (Ballentine et al., 1991; Sherwood Lollar et al., 1997), complex geodynamic setting (Horváth et al., 2015) and volcanic activity (Harangi and Lenkey, 2007) that have developed within a relatively short time scale of 16 My (Kovács and Szabó, 2008). The PB represents an ideal setting for studying the fluxing of mantle CO_2 through the lithosphere. This study develops an innovative multi-technique approach in order to investigate the abundance and significance of CO_2 fluid inclusions and vesicles within mantle xenoliths by coupling: (1) three-dimensional synchrotron X-ray microtomography, (2) nanoSIMS, Raman spectroscopic and microthermometric characterization and (3) thermodynamic modeling of the magmatic evolution.

2 Geological background

The Pannonian Basin (PB) is located in the Carpathian–Pannonian region of Central Europe. The PB is a typical inter-arc basin (Embey-Isztin et al, 2001), yet it shows a number of features that are characteristic of rift zones, such as high heat flow, recent alkali volcanism, thin crust and lithosphere, and upwelling asthenosphere (Embey-Isztin et al., 1990; Praus et al., 1990; Spakman, 1990; Falus et al., 2007). The Pannonian Basin experienced a complex geodynamic evolution during the Miocene to Pleistocene characterized by the succession of extension-compression-extension events (Bali et al., 2008). The major driving forces that led to the formation of the Pannonian Basin (~20 Ma) were the continuous subduction and roll-back on its eastern boundaries and the synchronous eastward extrusion of ALCAPA blocks (Kazmer and Kovacs, 1985) from the Alpine compressional belt (Horvath, 1993; Fodor et al., 1999).

The Bakony–Balaton Highland Volcanic Field (BBHVF), on the northern shore of Lake Balaton, is situated near the center of the Carpathian-Pannonian region, in the western Pannonian Basin (western Hungary). The volcanic centers of the BBHVF were active between 7.96 Ma and 2.61 Ma (Balogh and Pécskay, 2001; Balogh and Németh, 2005; Wijbrans et al., 2007; Hidas et al., 2010) and produced mostly alkali basaltic volcanic rocks (Szabó et al., 1992; Embey-isztin et al., 1993).

Ultramafic xenoliths can be found in basanitic lava flows and pyroclastic volcanic products at six locations (Tihany, Bondoró Hill, Füzes-tó, Szentbékkálla, Mindszentkálla, Szigliget). Most of the xenoliths are spinel lherzolites, but harzburgite, clinopyroxenite, orthopyroxenite, wehrlite, websterite and, sometimes, composite xenoliths also occur (See Creon et al. (this volume) for more information).

3 Petrography of the mantle xenoliths

More than 150 ultramafic xenoliths from the BBHVF were collected at the Szentbékkálla, Szigliget,Füzes-tó and Mindszentkálla localities (see Creon et al. (this volume) for sampling locations). After microscopic observations, four ultramafic xenoliths from Szentbékkálla, one from Szigliget and two from Füzes-tó were selected for further study. Samples selected are 7 to 12 cm long, rounded spinel peridotites and range from lherzolite to harzburgite compositions. A detailed petrographic description of the samples is given in the companion paper by Creon et al. (this volume), and only a short description will be given here. Further petrographic observations obtained by X-ray tomography will be presented in the *Results* section. Peridotite samples show equigranular to mosaic or protogranular microstructures with minor poikilitic features (based on the classification of Mercier & Nicolas (1974)). Samples are composed of olivine (Ol), orthopyroxene (Opx), clinopyroxene (Cpx) and spinels (Sp). Amphibole (Amp) also occurs in some of the xenoliths (Szigliget and Füzes-tó). Microscopic observations show that the majority of these xenoliths contain veins, primary silicate melt inclusions or melt pockets. Melt pocket sizes are variable (from few hundreds microns to few millimeters in diameter) and are usually connected to each other by thin silicate melt veins. The melt pockets are composed of secondary formed clinopyroxene, olivine, spinel, and interstitial glass with vesicles. Melt pocket shapes can be irregular, but some are euhedral pseudomorphs of protominerals (amphibole). Numerous trails of secondary fluid inclusions are observed in Opx, Cpx and Ol. Fluid inclusions display equilibrium and non-equilibrium features depending on the samples (Creon et al.,this volume).

3.1 Analytical methods

150 3.1.1 Synchrotron X-ray microtomography

151

152 The eleven samples analyzed consist of tiny cylinders 5 to 10 mm in length and 4 mm in
153 diameter (Fig. 1). The internal textures of the mantle xenoliths were characterized through
154 synchrotron radiation computed micro-tomography at the European Synchrotron Radiation
155 Facility (ESRF), Grenoble (France) on the ID19 beamline. ESRF offers access to very high
156 X-ray beam intensity. The detector used is a Fast Readout Low Noise FRELON Camera
157 developped at ESRF, with 2048×2048 pixels and 14 bits resolution (Baruchel et al., 2000;
158 Labiche et al., 2007).
159 Monochromatic microtomography with 30 keV radiation was done on the 4 mm diameter
160 cylinders, using a multilayer monochromator. The phase contrast effect was obtained with a
161 short propagation distance; the sample-detector distance was of 10 mm for a pixel size equal
162 to 1.27 µm. With this setting (Fig. 1), scanned regions were 4 mm by 2 mm in size when
163 using a half-acquisition mode. Typically, the 3D images obtained are composed of
164 3639×3639×2048 voxels (elementary image volume) with 32-bit grey-scale resolution.
165 Acquisition time was of the order of 45 min for 5000 projections together with around 625
166 reference images (blanks). A primary correction of the ring artifacts was done directly after
167 analysis using specific filtering. Tomographic volume reconstructions (example given in Fig.
168 2) were performed using an algorithm with a single phase retrieval distance in order to
169 optimize the signal/noise ratio (Paganin et al., 2002; Sanchez et al., 2012). Petrographic data
170 treatments were performed using ImageJ® and Avizo® softwares. Individual grey levels were
171 identified for each solid (mineral and glass), liquid and gas phase by defining their threshold
172 bracketing on bulk sample grey level histograms calculated using ImageJ® (Fig. 3). Then the
173 3-D volumes of each petrographic phase were defined with the Avizo® software. Each phase
174 was individualized by segmentation of the volumes corresponding to their density range.

Uncertainties associated with this segmentation were qualified by manually adjusting minimum and maximum thresholds for each phase (Fig. 4). Once the thresholds well defined, the volumes of the phases were segmented and quantified.

The densities of the petrographic phases were calculated from their grey levels using model absorbance compiled with a NIST utility (http://www.nist.gov/pml/data/xcom/).

3.1.2 Nano-SIMS microanalyses of C and H

Carbon and water contents of glass were determined using the NanoSIMS 50 installed at the MNHN (Paris) on gold-coated (10 nm thick) samples. Analyses were performed with a 16 keV Cs+ primary ion beam rastering the surface of the sample. A primary beam intensity of 40 pA was used to perform analyses with a D1-3 (200 µm) aperture diaphragm. Secondary ions of ^{12}C, $^{16}O^{1}H^{-}$, $^{28}Si^{-}$, $^{27}Al^{16}O^{-}$ and ^{56}Fe were collected using electron multipliers over 3 x 3 µm² square using the beam blanking mode (1.5 x 1.5 µm²) to reduce surface contamination (Stephant et al., 2014). A presputtering on a 3 × 3 μm^2 surface area during 300 s was performed to remove coating and initial surface contamination and to reach the sputtering steady-state. Calibration curves were obtained by measuring tholeiitic glass standards (Fig. 5) provided by the Centre de Recherche en Pétrographie et Géochimie (CRPG), Nancy, France [standard description available in Shishkina et al. (2010)]. Data corrections, using the aforementioned calibration, and error calculations were performed using the R program (Dunn, 2007). Errors combine counting statistics and uncertainty of the calibration curve. However, the errors reported in Table 1 are dominated by the uncertainty of the calibration curve, which corresponds to prediction interval at 68% (1σ) (Bartoli et al., 2014). During the session, the vacuum in the analysis chamber remained at 5×10^{-10} Torr.

200 3.1.3 Raman Spectroscopy and Microthermometry

201

202 3.1.3.1 Raman Spectroscopy

203

204 The fluid inclusions (trapped by order of abundance in Opx, Cpxand Ol) were analyzed (n=
205 99) by Raman spectroscopy at Faculty of Science Research and Instrument Core Facility
206 (ELTE FS-RICF, Hungary). A Jobin Yvon confocal Labram Raman instrument was used with
207 a frequency-doubled Nd-YAG laser with an excitation wavelength of 532 nm. Laser energy
208 was 50 mW and 20 mW at the laser source and at the sample surface, respectively. 50× and
209 100× microscope objectives were used to focus the laser onto the sample and to collect the
210 Raman signal. Analytical settings included a 200–500 μm confocal hole, 200 μm spectral slit,
211 600 or 1800 grooves/mm spectrograph gratings, 2–10 accumulations and 2–150 s acquisition
212 time (all depending on the maximum intensity). The spectral resolution of the measurements
213 varied with wave number but was ≤2 cm^{-1} using the grating with 1800 grooves/mm.
214 Following the method of Berkesi et al. (2009), spectra were collected at room and high
215 (150°C) temperatures using a Linkam THMS600 heating/cooling stage. To characterize the
216 bands in the Raman spectra and to identify the phases present, data were compared to the
217 online Raman database of the French Society of Mineralogy and Crystallography
218 (http://wwwobs.univ-bpclermont.fr/sfmc/ramandb2/index.html) and to that of Bonelli &
219 Frezzotti (2003), http://www.dst.unisi.it/geofluids/raman). Data were processed using
220 LabSpec v5.25.15 software designed for Jobin-Yvon Horiba LabRam instruments. Minimum
221 and maximum values of CO_2 densities in inclusions were calculated from the two Raman
222 bands of CO_2 due to Fermi resonance (Fall et al., 2011) (Fig. 6).

223

224 3.1.3.2 Microthermometry

A Linkam MDS 600 heating-freezing stage (IFP Energies nouvelles, Rueil-Malmaison, France) was used to measure the phase transitions in CO_2-rich fluid inclusions, which homogenized in the liquid phase in our samples. After freezing the fluid at <-75 °C, the inclusions were slowly heated to the triple point temperature check (-56.6 °C for pure CO_2) with a heating rate of 0.5-2 °C.min^{-1}. Final homogenization occurred to the liquid phase (T_hL). The CO_2 density and pCO_2 were calculated following Span and Wagner, 1996 and Sterner and Pitzer, 1994, respectively, for a magma temperature of 1150 ± 15 °C (estimation from Creon et al. (this volume) from the melting conditions.

3.2 Results

3.2.1 Synchrotron X-ray tomography

3.2.1.1 Petrographic observations

The density resolution of synchrotron X-ray tomography allows clear discrimination among the six major phases of the peridotitic xenoliths: olivine, orthopyroxene, clinopyroxene, spinel, glass and fluid. Figure 3 shows the density spectra of the SZB51 xenolith together with the modal composition corresponding to the pixel count of each phase. In SZB51 (Fig. 3), olivine is the most abundant phase and fluid is the least abundant.

Regarding the 3D images obtained by synchrotron X-ray microtomography, we confirm that the rock textures are protogranular, tabular or equigranular-mosaic (according to the classification of Mercier & Nicolas, 1974) as previously reported by optical microscopy on thin sections of the same samples (Creon et al., this volume).

The glass phase may be located at grain boundaries as veins or melt pockets (Fig. 6). Fluids are observed as trails of secondary fluid inclusions (FI) inside minerals (Ol, Opx, Cpx) or as vesicles inside the glass (Fig. 6e). Glass containing vesicles forms a complex interconnected network along grain boundaries as shown in figure 7. Trails of FI run across pre-existing melt veins and melt veins cross pre-existing trails of FI. Moreover, trails of secondary FI and the glass (+ vesicles) network intersect each other through multiple grains. Small (~100-200 µm, Fig. 8) newly formed Ol, Cpx and Sp are observed in veins (in low abundance) and in melt pockets (in high abundance).

The glass (+ vesicle) network percolates through the whole volume and is in direct contact with the exterior, indicating that vesicles probably lost all the gas they previously contained during their exposure to surface conditions or during sample preparation.

3.2.1.2 Phase volume quantification

The volumes of minerals, glass and fluid phases have been quantified within the bulk 3-D volumes. Fluid volumes have been calculated on each sample by direct density threshold segmentation; the obtained volumes are between 0.7 and 4.7 vol% (Fig. 9a & Table 1). Vesicles in melt systematically make the majority of the fluid volume, FIs representing at most 5 vol. %. The FIs can be divided according to which mineral they are hosted in. In sample SZB51, for example, FI represent a volume proportion in opx of 0.6%, in cpx of 0.3%, and in ol of 0.18%. These proportions, weighted by the modal composition of SZB51, imply that opx, ol and cpx trapped respectively 57.8%, 39.0% and 3.3% of the total FI volume (Fig. 9b).

Glass volume determination was performed in two steps. The first step resulted from the glass volume calculation by direct threshold segmentation (as for fluid volumes) and gave volumes

between 0 and 3.8 vol% (best estimate). The second step was performed for some samples (SZB50, SZG23, FT12 and FT01P) that showed evidence of important secondary crystallization of the melt (quenched as glass) such as newly formed Ol, Cpx and Sp (Fig. 8). In order to correct the glass volumes from this crystallization of new phases, and to consider the pre-crystallized bulk volume of melt pockets, we extracted the X-ray images of silicate melt pockets on five slices of each sample and calculated their (melt+newly formed minerals)/melt volume ratios (Fig. 8). The obtained ratios were used to correct the 3D glass volumes from crystallization of new phases. The corrected glass volumes in these samples range between 0 and 23.4 vol. % of the total volume (Fig. 9a, Table 1).

The corrections for crystal fractionation were performed only on silicate melt pockets since veins only show very minor crystallization that should have negligible effects on the melt volumes. After correction for crystallization of newly formed phases in the melt pockets, the glass and the fluid volumes display a linear correlation (Fig. 11).

3.2.1.3 Density determination

The grey level value of each pixel was quantitatively assigned to a density. Densities determined for Ol (3.37 to 3.41 $g.cm^{-3}$), Opx (3.29 to 3.32 $g.cm^{-3}$) and Cpx (3.42 to 3.43 $g.cm^{-3}$) correspond to those described in the literature using the Mg# of the minerals of these samples Creon et al. (this volume) (Fig. 11). Glass densities were then determined using the average density of glass-assigned pixels in each sample. The densities are distributed between 2.45 and 2.74 $g.cm^{-3}$ (Table 1, Figure 11) and are in agreement with andesite to basalt glass densities available in the literature (Richet et al. 2000 and references therein). Densities calculated with the method of Dixon et al. (1995) (2.41 to 2.59 $g.cm^{-3}$) are also close to those

299 determined in this study (Fig. 11). Glass densities determined by X-ray microtomography are
300 therefore considered to be accurate and will be used in the following steps of this study.
301 The X-ray microtomography density determinations for the fluid vesicles and inclusions were
302 not conclusive due to the poor X-ray absorbance resolution in the lower density range
303 (typically 0 to 1.5 g.cm^{-3}), together with the partial-volume-effects (density artifact due to the
304 presence of a phase boundary within a single voxel) on the smaller segmented volumes, which
305 commonly affect the fluid/solid phase boundaries.
306
307 3.2.2 Fluid compositions and densities
308
309 Fluid compositions and densities were measured on FI by Raman spectroscopy and
310 microthermometry. As noted above, fluids originally trapped in vesicles in the melt veins and
311 melt pockets were lost from the sample and could not be analyzed; hence the FI were used as
312 representatives of all the fluids of the samples, even though the vesicles dominated the
313 volume fraction assigned to fluid. Following the method developed in Berkesi et al. (2009),
314 we used Raman spectroscopy at room and elevated temperatures (150 °C) in order to
315 discriminate the potential trace volatiles inside fluid inclusions. With this method, only CO_2
316 was recognized in the fluid inclusions. Independently, the phase transition observed at ~56.6
317 ± 1 °C by microthermometry measurements is in agreement with pure CO_2 inclusions.
318 The comparison of densities obtained with both Raman spectroscopy and microthermometry
319 methods shows a linear correlation, with a correlation factor of 0.89 (R^2). This suggests that
320 the fluid density datasets obtained by the two methods are internally consistent (Fig. 14a). The
321 densities of fluids obtained in SZB, SZG and FT are respectively between 0.30 and 1.11 g.cm^{-3},
322 0.48 and 0.82 g.cm^{-3} and 0.30 and 1.06 g.cm^{-3} (Fig.13b).
323

3.2.3 Volatiles dissolved in glass

NanoSIMS analyses have been performed on glass from veins and melt pockets to determine their CO_2 and H_2O contents. H_2O contents vary from 0.54 ± 0.26 (1σ) to 4.25 ± 0.27 (1σ) wt. % in glass from veins and from 0.55 ± 0.26 (1σ) to 2.76 ± 0.28 (1σ) wt. % in glass from melt pockets. CO_2 contents vary between 0.27 ± 0.01 (1σ) and 0.48 ± 0.02 (1σ) wt. % in glass from veins and from 0.38 ± 0.01 (1σ) to 0.96 ± 0.02 (1σ) wt. % in glass from melt pockets (Table 1).

4 Discussion

4.1 Magma CO_2-supersaturation conditions

Several petrographic lines of evidence point to CO_2 supersaturation in the melt trapped within the studied xenoliths at lithospheric depths. Such evidence includes 1) the occurrence of CO_2 FI with densities above 1.0 g.cm^{-3} (Table 1) corresponding to pressures higher than the present Moho depth (25-30 km, Kovacs et al., 2012); 2) the coexistence within veins of vesicles and glass with high dissolved CO_2 and H_2O concentrations in the glass of up to 0.96 and 4.25 wt. %, respectively (Table 1). In order to assess the conditions of magma supersaturation, CO_2 saturation isotherms were calculated for the different melt compositions measured in the present samples over a range of assumed temperatures using the Rhyolite-MELTS software (version 1.2.0, Gualda et al., 2012; Ghiorso and Gualda, 2015). This model is suitable for the calculation of thermodynamic equilibrium of mafic to felsic systems with H_2O and CO_2 over the pressure range 0-3 GPa, corresponding to the conditions of the lithospheric mantle below the BBHVF (Kovacs et al., 2012).

Magma CO_2-saturation shows little temperature dependence between 1100 and 1300 °C and for pressure below 0.5 GPa, as already shown by Shishkina et al. (2010) and Botcharnikov et al. (2006). The effect of temperature only tends to increase the solubility of CO_2 in the high pressure range of 0.5-3.0 GPa, as also mentioned by Papale et al. (2006). Based on CO_2-saturation isotherms, vesicle-melt equilibrium pressures were calculated from the CO_2 contents of melts determined by NanoSIMS (Table 1, Figure 13). These saturation pressures at 1100°C (corresponding to approximated mineral equilibrium temperatures determined in Creon et al. (this volume)) vary between 0.69 and 1.78 GPa and correspond to depths of 26 to 62 km (using the geotherm of Kovacs et al., 2012). Such estimations likely correspond to vesicle-melt equilibrium near the glass transition during rapid cooling of the percolating melt within the melt veins and pockets. Glass transition temperatures (Tg) were estimated between 670 to 854°C by Giordano et al. (2008) at asthenospheric pressures, and between 520 to 930°C by Morizet et al. (2007) at pressures between 1.0 and 2.5 GPa (phonolite melts). CO_2 appears to have almost no effect on the glass transition of silicate melts unlike H_2O, which clearly reduces glass transition temperatures (Morizet et al. 2007). Furthermore, pressure has a very limited influence on glass transition temperatures as demonstrated by Bagdassarov et al. (2004). These glass transition temperatures would be intersected along the geotherm of Kovacs et al. (2012) at pressures near ~0.5 GPa i.e. at crustal levels (~20 km depth). Because melt pockets were shown to have been quenched under lithospheric mantle pressures while coexisting with fluid vesicles (Creon et al., this volume), the crustal saturation pressures recorded for most CO_2 depleted melts are likely to reflect the fast ascent of xenoliths after their extended residence time at lithospheric mantle depths.

Melt saturation pressures of 0.69 to 1.78 GPa were converted to CO_2 density using the equations of state of Span & Wagner (1996) and Sterner & Pitzer (1994). The densities obtained vary between 0.93 and 1.33 $g.cm^{-3}$ and are consistent with the density range

374 determined by Raman spectroscopy and microthermometry in the denser FIs (Table 1). This
375 similarity attests to a coeval formation of FI and vesicles at lithospheric mantle conditions.
376 However, no direct correlation is observed between maximum fluid inclusion and vesicle
377 densities, which likely points to the unstable behavior of highly over-pressurized FIs
378 (Roedder, 1984). In most cases (samples SZB16, SZB50, SZG23, SZG44, FT12), fluid
379 inclusion densities are lower than the associated calculated vesicle densities; which can occur
380 due to the decrepitation of the FIs during xenolith ascent (Bodnar, 2003). In the rest of the
381 xenoliths (SZB51, SZB52, FT01P) the densities of the FI are larger than those of the
382 associated vesicles, which reflects FI trapping in equilibrium with vesicles at pre-ascent
383 lithospheric mantle pressures.
384 In figure 14, the CO_2 contents dissolved in glass measured by NanoSIMS (0.27-0.96 wt. %)
385 are compared with the data compilation of Wallace (2005). The values measured in this study
386 are in excess of those reported so far for arc magmas and are within the E-MORB range.
387 Moreover, the CO_2 and H_2O contents measured are larger than those described in the
388 literature in silicate melt pockets of the BBHVF (Bali et al., 2002). Hidas et al. (2010) used
389 silicate melt inclusions (SMI) from Szigliget mantle xenoliths to estimate the volatile content
390 of trapped metasomatic melt. Their calculated melt CO_2 concentrations of ~1 wt. % are in
391 agreement with the maximum CO_2 content measured in glass for this study in sample SZG23
392 from the same xenolith locality (0.8-1.2 wt. % CO_2; Fig. 14). It is thus likely that the SMI
393 analyzed by Hidas et al. (2010) correspond to the trapping of a volatile-rich melt during
394 overgrowth of clinopyroxenes in the mantle lithosphere similar to the most CO_2-rich
395 percolating melts analyzed in this study.
396
397 4.2 CO_2 contents of melts in the subcontinental lithosphere beneath the BBHVF
398

399 The 3-D images clearly reveal interconnections between trails of secondary fluid inclusions,
400 the glass in veins and in melt pockets and the network of vesicles. This is contrary to
401 observations made in similar samples from the same localities by Demény et al. (2010), who
402 described trails of FI in thin sections that did not extend to grain boundaries. The synchrotron
403 X-ray microtomography used in this study allows 3-D reconstructions that show indisputable
404 intersecting relationships of FI trails with grain boundaries (Figure 7). These 3-D observations
405 are clear petrographic evidence for a common fluid being present in the FI and in the
406 metasomatic melt that percolated these mantle xenoliths. As noted above, fluid in vesicles are
407 not preserved anymore and are, therefore, impossible to identify. Hence, we assumed that
408 vesicles have similar compositions as FIs and that they are dominated by CO_2. This
409 assumption is consistent with the high H_2O and CO_2 contents in the glass determined by
410 nanoSIMS.
411 The CO_2/glass mass ratio corresponding to the melt + vesicle system has been calculated
412 using equation (1):
413
414 *(1)* $M(CO_2)/M(Glass) = V(CO_2)/V(Glass) * \rho(CO_2)/\rho(Glass)$
415
416 Where: *$M(CO_2)$: mass of CO_2; M(Glass) : mass of glass; $V(CO_2)$: volume of CO_2 ; V(Glass) : volume*
417 *of glass ; $\rho(CO_2)$: density of CO_2 ; ρ(Glass) : density of glass*
418
419 $V(CO_2)$, $V(glass)$ and $\rho(glass)$ were obtained by synchrotron X-ray microtomography and
420 $\rho(CO_2)$ was derived from the NanoSIMS analyses and thermodynamic modeling (Rhyolite-
421 MELTS, Gualda et al. 2012; Ghiorso & Gualda 2015) as described in the previous section
422 (Table 1).
423 The calculated CO_2/melt mass ratios range from 9.0 to 25.4 wt. % (Table 1). These ratios,
424 which can be considered as the CO_2 mass fraction of the entire melt system, would

correspond to a single phase system at pressures of 4 to 9 GPa for basaltic melts following the study of Guillot & Sator (2011). The present lithosphere-asthenosphere boundary below the Pannonian Basin is estimated at depths between 60 and 100 km (Tašárová et al., 2009). The melts characterized here were therefore likely to be supersaturated in the asthenosphere before reaching lithospheric depths. The range of CO_2/melt mass ratios calculated in this study implies that CO_2 contents in melts were variable either due to magmatic processes or to physical fractionation. Below we review the various processes that might affect the CO_2/melt ratio in lithospheric melts.

4.2.1 Carbonate assimilation and fractionation in the lithospheric mantle

Carbonate minerals have been described in Pannonian Basin xenoliths from the BBHVF. These carbonates are mainly calcitic droplets (Demény et al., 2004), rounded (Bali et al. 2002; 2008) or anhedral (Chalot-Prat and Arnold, 1999) crystals in silicate veins and/or melt pockets of mantle xenoliths. In the samples of this study, carbonate are also observed as veins (Creon et al., this volume). Bali et al. (2002) and Demény et al. (2004) suggested the infiltration of a mixed carbonate–silicate melt taking place in these mantle xenoliths, which supports the evidence for CO_2-rich magma percolation beneath the BBHVF documented in this study. Carbonates are, therefore, not the source of the melts but instead precipitate from a CO_2-rich metasomatic agent during melt-rock reactions due to carbon saturation and vapor immiscibility in the percolating silicate melts. Thus, the variability in CO_2 mass fractions in melts calculated in this study is not believed to be caused by variable dissolution of carbonated peridotites in the lithospheric mantle.

Reversely, the fractionation of carbonate minerals, or phase separation of carbonate and silicate melts may have potentially played a role in fractionating CO_2 mass fractions in

magmas. Since no evidences of carbonate fractionation, nor carbonate melt segregation have been witnessed in our sample set, although they were observed and discussed in comparable samples of xenoliths of Transylvania (Chalot-Prat and Arnold, 1999; Bali et al., 2002; Demény et al., 2004; Bali et al., 2008) we suggest that such processes were not the driving mechanisms of the observed heterogeneity in the CO_2 mass fraction.

4.2.2. Fluid inclusions and physical fractionation

The large abundance of CO_2-rich FIs trapped in minerals along fractions and the absence of comparably abundant silicate melt inclusions indicate that CO_2 was preferentially trapped in grains in comparison with the silicate melt.

Schiano et al. (2006) suggested that the occurrence of fluid inclusion arrays, commonly observed in mantle xenoliths, could be explained by transcrystalline melt migration, contrary to the commonly accepted idea of simple trapping by "crack and seal" processes of individual or multiple mineral grains of a free fluid phase percolating the deep mantle. However, no textural features suggesting transcrystalline melt migration were observed in our samples. Schiano et al. (2006) explained that only the most primitive droplets formed at fertile grain corners (or edges) have time (if melting does not proceed rapidly to higher degrees) to enter the crystals by thermally driven migration instead of escaping by buoyancy-driven flow along grain edges. Melts analyzed in this study have evolved compositions (55.96-62.71 wt. % SiO_2), consistent with the formation of an interconnected wet-edge network and rapid escape to higher levels, where grain scale channels are relayed by fracture networks to form magma bodies (Schiano et al., 2006). The absence of the high thermal gradient (0.03 to 0.06 K/μm) needed for transcrystalline melt migration (Schiano et al., 2006) could also explain the absence of evidence of transcrystalline melt migration in the mantle xenoliths studied here.

475 The microstructures observed in samples from this study suggest that peridotites are wetted by
476 silicate melt and not by CO_2 as already indicated by several authors (e.g. Watson & Brenan,
477 1987). This observation is consistent with the much smaller wetting angles expected for
478 silicate melt in dunite than for CO_2 in dunite (Watson & Brenan, 1987). Consequently, melt
479 inclusions only rarely trap melts with their primary CO_2 contents (e.g., Saal et al. 2002).
480 Instead, grain fractures due to mantle dynamic or to local overpressure may much more easily
481 trap volatiles as FI due to preferential viscosity-controlled injection within grain cracks
482 (Watson and Brenan, 1987). We suggest that cracking and healing processes operating in
483 response to fluid overpressure and creeping of the peridotite matrix induced the preferential
484 entrapment of CO_2 in minerals whereas the silicate melt from the same magma continued its
485 journey at grain boundaries through percolation. Variable amplitudes of this fractionation
486 process may then be expected depending on magma travelling distances, melt/rock ratios and
487 fluid overpressure conditions.
488
489 4.3 Trapped lithospheric melts in mantle xenoliths and arc magmas
490
491 Creon et al. (this volume) interpreted the metasomatic agent that infiltrated these xenoliths to
492 be a CO_2-rich adakite-like magma derived from slab melting that interacted with the
493 lithosphere mantle before being trapped in the peridotites. Wallace (2005) compiled the CO_2
494 and H_2O contents of silicate melt inclusions deduced from arc-magmas worldwide, which
495 range between 0 and 2100 ppm and between 1.9 and 6.3 wt. % respectively (Figure 15). The
496 CO_2 concentrations are much lower than the values determined in this study, which range
497 from 0.29 to 0.96 wt. % and are much higher than that of SMI in arc magmas worldwide. The
498 H_2O contents determined in this study range from 0.54 and 4.25 wt. % and are for the
499 majority, in the same range as those reported by Wallace (2005). We suggest that the CO_2

content of arc magmas sampled by SMIs may only represent a negligible fraction of the CO_2 associated with slab-derived melts. For instance, in xenoliths from this study as well as in those from the literature (Bali et al. (2008) and Hidas et al. (2010)), only a very small fraction of the CO_2-rich melt may be trapped as SMIs due to the pre-entrapment supersaturation in CO_2 and the preferential accumulation of most of the CO_2 in vesicles and FIs (95-98 % in samples from this study) rather than in the silicate melt. A large compositional gap seems to exist in subduction-related environments between CO_2/magma mass fractions trapped as melts in the lithospheric mantle and melts characterizing erupting subduction-related magmas. This gap may be the result of physical and/or geochemical processes such as 1) intense physical fractionation of CO_2 vesicles and silicate melt during magma ascent to the crust, 2) important dilution of CO_2-rich parental magmas by assimilation of C-poor lithologies during magma-rock interaction. The investigation of these processes is however beyond the scope of this paper and will not be discussed further here.

Figure 15 illustrates the different potential sources of H_2O and CO_2 expected in a subduction context where 1) E-MORB, 2) altered oceanic basalts and 3) subducted sediments (Plank and Langmuir, 1998; Wallace, 2005) represent rock-type end-members of slab melting. Partial melting of the slab or of the metasomatized mantle wedge would generate melts enriched in incompatible trace elements and with high CO_2 and H_2O contents like those calculated in this study (0.55-4.25 wt. % H_2O and 9.0-25.4 wt. % CO_2; Figure 15 and Table 1). If the CO_2 content of the melt is converted into carbonate content at the source (which implies congruent melting of the source), the latter could have contained up to 20-40 wt. % of carbonate. Dasgupta et al. (2013) experimentally showed that carbonated silicate melt with 15-25 wt. % CO_2 and a modest amount of water (1-5 wt. %) can be generated in the upper part of the asthenospheric mantle (1,300-1,750 °C and 2-5 GPa) and is able to percolate upward the lithospheric mantle. We conclude that the high CO_2/melt ratios determined in this study

correspond to deep melts derived from slab melting, which have percolated to lithospheric depths without having been substantially fractionated.

4.4 A lithospheric carbon reservoir?

The mass ratios of CO_2/peridotite have been calculated for each xenoliths which provide values between 2700 and 24,400 ppm by weight of CO_2 with an average of about 9557 ppm. This is considered representative of the average quantity of carbon stored in the samples examined. However, the present study is based on fluid inclusion-rich samples only, which correspond to ~20 % of an initial sample set of collected mantle xenoliths. If we make a conservative assumption that the remaining 80% of the initial sample set contains on average 30 ppm carbon, a typical estimate for the N-MORB mantle (Marty, 2012), then we can deduce a first order estimate of the CO_2 content present in the Pannonian lithospheric mantle. Thus, we estimate that quantity to be 1935 ppm CO_2 (0.2 x 9557 ppm + 0.8 x 30 ppm = 1935 ppm). We consider this first order CO_2 content as representative of the bulk lithospheric mantle sampled by the alkaline volcanism of the BBHVF. This estimate is within a factor of two of the 1000 ppm estimated by Kelemen & Manning (2015) for back-arc lithospheric mantle based on observed carbon fluxes and reservoirs at subduction zones. For comparison, the carbon content at source regions of MORB is thought to be bound between 50 and 200 ppm, whereas the source mantle of OIB is richer and may have be between 1000 and 4000 ppm CO_2 (Marty and Tolstikhin, 1998; Saal et al., 2002; Pineau et al., 2004; Cartigny et al., 2008). We suggest that the quantitative peridotite + melt + volatile characteristics described here, and found in many other regions of the Earth, may be representative of the carbon reservoir residing in the lithospheric mantle, at least for back-arc areas.

549 Besides the implications of our findings for the carbon cycle, such a lithospheric carbon
550 reservoir has several consequences for the degassing of mantle volatiles in active geodynamic
551 settings such as the Pannonian Basin, where mantle-derived CO_2 outgassing through the
552 Pannonian Basin sedimentary rocks is observed (Ballentine et al., 1991). This suggests that
553 the carbon reservoir of at least ~2000 ppm quantified in this study is transient, and may be
554 recycled to the atmosphere and to the asthenosphere over geodynamic timescales by passive
555 tectonic degassing, active volcanism or delamination.
556
557 5 Conclusions
558
559 The magmatic-CO_2 budget of the subcontinental lithospheric mantle below the Pannonian
560 Basin has been constrained by coupling synchrotron 3-D X-ray microtomography, nanoSIMS,
561 Raman spectroscopy, and microthermometry in combination with thermodynamic modeling
562 in order to investigate the significance of abundant CO_2–rich fluid inclusions, CO_2-bearing
563 glass and vesicles within lithospheric peridotite xenoliths.
564 3-D volume reconstructions allow quantifying the proportions of all mineral phases in the
565 xenoliths and their textural relationships. Interconnection between trails of secondary fluid
566 inclusions and the network of glass + vesicles demonstrates a common fluid composition
567 between fluid inclusions and melt percolation in these mantle xenoliths. The vapor phase
568 volume (vesicles + fluid inclusions) observed requires CO_2-supersaturation of the silicate
569 melts, which allows to calculate melt saturation pressures based on the dissolved CO_2 content
570 of the glass.
571 The CO_2/glass mass ratio corresponding to the melt + vesicle system is estimated from the
572 microtomography, NanoSIMS analyses and thermodynamic modeling. The CO_2/melt mass
573 ratios obtained range from 9.0 and 25.4 wt. % and are related to a slab-derived melting

source. A first estimate of ~1935 ppm CO_2 for the Pannonian Basin lithospheric mantle is proposed and can be considered as representative of the bulk lithospheric mantle sampled by the alkaline basalt volcanism of the BBHVF.

This petrologic and geochemical approach is the first direct quantification of the bulk carbon content in the lithospheric mantle, and is in agreement with independent lines of reasoning suggesting a large transient reservoir of carbon in the lithospheric mantle near subduction-arc systems. Further quantification of the volume, residence time, and general significance of this reservoir requires more systematic regional and global studies using similar approach.

6 Acknowledgements

This project was funded by IFP Energies nouvelles. The European Synchrotron Research Facility of Grenoble, the ID19 beamline team and more specifically Paul Tafforeau are thanked for their financial and technical support. The National NanoSIMS facility at the MNHN was established by funds from the CNRS, Région Ile de France, Ministère délégué à l'Enseignement supérieur et à la Recherche, and the MNHN. We are grateful to Marie-Claude Lynch and Herman Ravelojaona for their precious assistance with X-ray tomography and sample preparations.

7 References

Anderson A. T. (1975) Some basaltic and andesitic gases. *Rev. Geophys.* **13**, 37.

Bagdassarov N. S., Maumus J., Poe B., Slutskiy A. B. and Bulatov V. K. (2004) Pressure dependence of T g in silicate glasses from electrical impedance measurements. *Phys. Chem. Glas. - Eur. J. Glas. Sci. Technol. Part B*, **45**, 197–214.

599 Bali E., Szabó C., Vaselli O. and Torok K. (2002) Significance of silicate melt pockets in
600 upper mantle xenoliths from the Bakony – Balaton Highland Volcanic Field , Western
601 Hungary. *Lithos* **61**, 79–102.
602 Bali E., Zanetti A., Szabó C., Peate D. W. and Waight T. E. (2008) A micro-scale
603 investigation of melt production and extraction in the upper mantle based on silicate melt
604 pockets in ultramafic xenoliths from the Bakony–Balaton Highland Volcanic Field
605 (Western Hungary). *Contrib. to Mineral. Petrol.* **155**, 165–179.
606 Ballentine C. J., O'Nions R. K., Oxburgh E. R., Horvath F. and Deak J. (1991) Rare gas
607 constraints on hydrocarbon accumulation, crustal degassing and groundwater flow in the
608 Pannonian Basin. *Earth Planet. Sci. Lett.* **105**, 229–246.
609 Balogh K. and Németh K. (2005) Evidence for the Neogene small-volume intracontinental
610 volcanism in Western Hungary: K/Ar geochronology of the Tihany Maar Volcanic
611 Complex. *Geol. Carpathica* **56**, 91–99.
612 Balogh K. and Pécskay Z. (2001) K/Ar and Ar/Ar geochronological studies in the Pannonian-
613 Carpathians-Dinarides (PANCARDI) region. *Acta Geol. Hung.* **44**, 281–299.
614 Bartoli O., Cesare B., Remusat L., Acosta-Vigil A. and Poli S. (2014) The H2O content of
615 granite embryos. *Earth Planet. Sci. Lett.* **395**, 281–290.
616 Baruchel J., Buffiere J.-Y., Maire E., Merle P. and Peix G. (2000) X-ray Tomography in
617 Material Science. *Hermes Sci. Publ.*
618 Berkesi M., Hidas K., Guzmics T., Dubessy J., Bodnar R. J., Szabó C., Vajna B. and
619 Tsunogae T. (2009) Detection of small amounts of H2O in CO2-rich fluid inclusions
620 using Raman spectroscopy. *J. Raman Spectrosc.* **40**, 1461–1463.
621 Bodnar R. J. (2003) Re-equilibration of fluid inclusions. *Fluid Inclusions Anal. Interpret.*
622 *Short Course Ser. Samson I, Anderson A, Marshall D Miner. Assoc Can, Vancouver* **32**,
623 213–231.

624 Bonelli R. and Frezzotti M. . (2003) Raman Spectra Database.
625 *http://www.dst.unisi.it/geofluidslab/Raman%20intro.html*.
626 Botcharnikov R., Behrens H. and Holtz F. (2006) Solubility and speciation of C–O–H fluids
627 in andesitic melt at T=1100–1300°C and P=200 and 500MPa. *Chem. Geol.* **229**, 125–
628 143.
629 Bruce Watson E. and Brenan J. M. (1987) Fluids in the lithosphere, 1. Experimentally-
630 determined wetting characteristics of CO2H2O fluids and their implications for fluid
631 transport, host-rock physical properties, and fluid inclusion formation. *Earth Planet. Sci.*
632 *Lett.* **85**, 497–515.
633 Burton M. R., Sawyer G. M. and Granieri D. (2013) Deep Carbon Emissions from Volcanoes.
634 *Rev. Mineral. Geochemistry* **75**, 323–354.
635 Cartigny P., Pineau F., Aubaud C. and Javoy M. (2008) Towards a consistent mantle carbon
636 flux estimate: Insights from volatile systematics (H2O/Ce, δD, CO2/Nb) in the North
637 Atlantic mantle (14° N and 34° N). *Earth Planet. Sci. Lett.* **265**, 672–685.
638 Chalot-Prat F. and Arnold M. (1999) Immiscibility between calciocarbonatitic and silicate
639 melts and related wall rock reactions in the upper mantle: a natural case study from
640 Romanian mantle xenoliths. *Lithos* **46**, 627–659.
641 Creon L., Delpech G., Rouchon V. and Guyot F. Melt-peridotite interaction in the lithospheric
642 mantle - Genesis of the Pannonian calc-alkaline suites revealed by Alkali basalt hosted
643 xenoliths. *this Vol.*
644 Dasgupta R. (2013) Ingassing, Storage, and Outgassing of Terrestrial Carbon through
645 Geologic Time. *Rev. Mineral. Geochemistry* **75**, 183–229. Dasgupta R. and Hirschmann
646 M. M. (2010) The deep carbon cycle and melting in Earth's interior. *Earth Planet. Sci.*
647 *Lett.* **298**, 1–13.
648 Dasgupta R., Mallik A., Tsuno K., Withers A. C., Hirth G. and Hirschmann M. M. (2013)

649 Carbon-dioxide-rich silicate melt in the Earth's upper mantle. *Nature* **493**, 211–215.
650 Demény A., Dallai L., Frezzotti M.-L., Vennemann T. W., Embey-Isztin A., Dobosi G. and
651 Nagy G. (2010) Origin of CO2 and carbonate veins in mantle-derived xenoliths in the
652 Pannonian Basin. *Lithos* **117**, 172–182.
653 Demény A., Vennemann T. ., Hegner E., Nagy G., Milton J. ., Embey-Isztin A., Homonnay Z.
654 and Dobosi G. (2004) Trace element and C–O–Sr–Nd isotope evidence for subduction-
655 related carbonate–silicate melts in mantle xenoliths (Pannonian Basin, Hungary). *Lithos*
656 **75**, 89–113.
657 Dixon J. E., Stolper E. M., Holloway J. R. and Science A. (1995) An Experimental Study of
658 Water and Carbon Dioxide Solubilities in Mid-Ocean Ridge Basaltic Liquids . Part II :
659 Applications to Degassing. *J. Petrol.* **36**, 1607–1631.
660 Dunn P. K. (2007) tweedie: Tweedie exponential family models.
661 Embey-Isztin a, Dobosi G., Altherr R. and Meyer H.-P. (2001) Thermal evolution of the
662 lithosphere beneath the western Pannonian Basin: evidence from deep-seated xenoliths.
663 *Tectonophysics* **331**, 285–306.
664 Embey-isztin A., Downes H., James D. E. E., Upton B. G. J. G. J., Dobosi G., Ingram G. A.
665 a., Harmon R. S. S. and Scharbert H. G. G. (1993) The petrogenesis of Pliocene alkaline
666 volcanic rocks from the Pannonian Basin, Eastern central Europe. *J. Petrol.* **34**, 317–343.
667 Embey-Isztin A., Sharbert H. G., Dietrich H. and Poultidis H. (1990) Mafic granulites and
668 clinopyroxenite xenoliths from the Transda- nubian Volcanic Region (Hungary):
669 implications for the deep structure of the Pannonian Basin. *Mineral. Mag.* **54**, 463–483.
670 Fall A., Tattitch B. and Bodnar R. J. (2011) Combined microthermometric and Raman
671 spectroscopic technique to determine the salinity of H2O–CO2–NaCl fluid inclusions
672 based on clathrate melting. *Geochim. Cosmochim. Acta* **75**, 951–964.
673 Falus G., Szabó C., Kovács I., Zajacz Z. and Halter W. (2007) Symplectite in spinel lherzolite

xenoliths from the Little Hungarian Plain, Western Hungary: A key for understanding the complex history of the upper mantle of the Pannonian Basin. *Lithos* **94**, 230–247.

Fodor L., Csontos L., Bada G., Györfi I. and Benkovics L. (1999) Tertiary tectonic evolution of the Pannonian basin and neighbouring orogenes: a new synthesis of palaeostress data. In: Durand, B., Jolivet, L., Horváth, F., Séranne, M. (Eds.), The Mediterranean Basins: Tertiary Extension with Alpine Orogen. *Geol. Soc.* **156**, 295–334.

Fyfe W. S., Price N. J. and Hompson A. B. (1978) Fluids in the Earth's Crust: Their Significance in Metamorphic, Tectonic, and Chemical Transport Processes. *Elsevier, Amsterdam*, 384 pp.

Ghiorso M. S. and Gualda G. A. R. (2015) An H2O-CO2 mixed fluid saturation model compatible with rhyolite-MELTS. *Contrib. to Mineral. Petrol.*

Giordano D., Russell J. K. and Dingwell D. B. (2008) Viscosity of magmatic liquids: A model. *Earth Planet. Sci. Lett.* **271**, 123–134.

Gorman P. J., Kerrick D. M. and Connolly J. a D. (2006) Modeling open system metamorphic decarbonation of subducting slabs. *Geochemistry, Geophys. Geosystems* **7**.

Gualda G. A. R., Ghiorso M. S., Lemons R. V. and Carley T. L. (2012) Rhyolite-MELTS: a Modified Calibration of MELTS Optimized for Silica-rich, Fluid-bearing Magmatic Systems. *J. Petrol.* **53**, 875–890.

Guillot B. and Sator N. (2011) Carbon dioxide in silicate melts: A molecular dynamics simulation study. *Geochim. Cosmochim. Acta* **75**, 1829–1857.

Hammouda T. (2003) High-pressure melting of carbonated eclogite and experimental constraints on carbon recycling and storage in the mantle. *Earth Planet. Sci. Lett.* **214**, 357–368.

Harangi S. and Lenkey L. (2007) Genesis of the Neogene to Quaternary volcanism in the Carpatian Pannonian region : Role of subduction , extension , and mantle plume. *Geol.*

699 *Soc. Am.* **Special Pa**, 67–92.
700 Hidas K., Guzmics T., Szabó C., Kovács I., Bodnar R. J., Zajacz Z., Nédli Z., Vaccari L. and
701 Perucchi A. (2010) Coexisting silicate melt inclusions and H2O-bearing, CO2-rich fluid
702 inclusions in mantle peridotite xenoliths from the Carpathian–Pannonian region (central
703 Hungary). *Chem. Geol.* **274**, 1–18.
704 Horvath F. (1993) Towards a mechanical model for the formation of the Pannonian Basin.
705 *Tectonophysics* **226**, 333–357.
706 Horváth F., Musitz B., Balázs a., Végh A., Uhrin a., Nádor A., Koroknai B., Pap N., Tóth T.
707 and Wórum G. (2015) Evolution of the Pannonian basin and its geothermal resources.
708 *Geothermics* **53**, 328–352.
709 Jarrard R. D. (2003) Subduction fluxes of water, carbon dioxide, chlorine, and potassium.
710 *Geochemistry, Geophys. Geosystems* **4**.
711 Johnston F. K. B., Turchyn A. V. and Edmonds M. (2011) Decarbonation efficiency in
712 subduction zones: Implications for warm Cretaceous climates. *Earth Planet. Sci. Lett.*
713 **303**, 143–152.
714 Kazmer M. and Kovacs S. (1985) ermian–Paleogene paleogeography along the Eastern part
715 of the Insubric–Periadriatic Lineament system: evidence for continental escape of the
716 Bakony- Drauzug unit. *Acta Geol. Hung.* **1-2**, 71–84.
717 Kelemen P. B. and Manning C. E. (2015) Reevaluating carbon fluxes in subduction zones,
718 what goes down, mostly comes up. *Proc. Natl. Acad. Sci.*, 201507889.
719 Kovacs I., Falus G., Stuart G., Hidas K., Szabó C., Flower M. F. J., Hegedűs E., Posgay K.
720 and Zilahi-Sebess L. (2012) Seismic anisotropy and deformation patterns in upper
721 mantle xenoliths from the central Carpathian–Pannonian region: Asthenospheric flow as
722 a driving force for Cenozoic extension and extrusion? *Tectonophysics* **514-517**, 168–179.
723 Kovács I. and Szabó C. (2008) Middle Miocene volcanism in the vicinity of the Middle

724 Hungarian zone: Evidence for an inherited enriched mantle source. *J. Geodyn.* **45**, 1–17.
725 Labiche J.-C., Mathon O., Pascarelli S., Newton M., Guilera Ferre G., Curfs C., Vaughan G.,
726 Homs A. and D. F. C. (2007) The fast readout low noise camera as a versatile X-ray
727 detector for time resolved dispersive extended X-ray absorption fine structure and
728 diffraction studies of dynamic problems in materials science, chemistry, and catalysis.
729 *Rev. Sci. Instrum.* **78**, 091301–091311.
730 Marty B. (2012) The origins and concentrations of water, carbon, nitrogen and noble gases on
731 Earth. *Earth Planet. Sci. Lett.* **313-314**, 56–66.
732 Marty B. and Tolstikhin I. N. (1998) CO2 fluxes from mid-ocean ridges, arcs and plumes.
733 *Chem. Geol.* **145**, 233–248.
734 Mercier J. C. and Nicolas A. (1975) Textures and Fabrics of Upper-Mantle Peridotites as
735 Illustrated by Xenoliths from Basalts. *J. Petrol.* **16**.
736 Morizet Y., Nichols A. R. L., Kohn S. C., Brooker R. a. and Dingwell D. B. (2007) The
737 influence of H2O and CO2 on the glass transition temperature: insights into the effects of
738 volatiles on magma viscosity. *Eur. J. Mineral.* **19**, 657–669.
739 Paganin D., Mayo S. C., Gureyev T. E., Miller P. R. and Wilkins S. W. (2002) Simultaneous
740 phase and amplitude extraction from a single defocused image of a homogeneous object.
741 *J. Microsc.* **206**, 33–40.
742 Papale P., Moretti R. and Barbato D. (2006) The compositional dependence of the saturation
743 surface of H2O+CO2 fluids in silicate melts. *Chem. Geol.* **229**, 78–95.
744 Pineau F., Shilobreeva S., Hekinian R., Bideau D. and Javoy M. (2004) Deep-sea explosive
745 activity on the Mid-Atlantic Ridge near 34°50′N: a stable isotope (C, H, O) study. *Chem.*
746 *Geol.* **211**, 159–175.
747 Plank T. and Langmuir C. H. (1998) The chemical composition of subducting sediment and
748 its consequences for the crust and mantle. *Chem. Geol.* **145**, 325–394.

749 Poinar K. (2012) The Carbon Cycle in the Mantle. , 1–11.
750 Praus O., Pěčová J., Petr V., Babuška V. and Plomerová J. (1990) Magnetotelluric and
751 seismological determination of the lithosphere-asthenosphere transition in Central
752 Europe. *Phys. Earth Planet. Inter.* **60**, 212–228.
753 Richet P., Whittington A., Holtz F., Behrens H., Ohlhorst S. and Wilke M. (2000) Water and
754 the density of silicate glasses. *Contrib. to Mineral. Petrol.* **138**, 337–347.
755 Roedder E. (1984) Fluid inclusions. *Rev. Mineral.* **12**.
756 Saal A. E., Hauri E. H., Langmuir C. H. and Perfit M. R. (2002) Vapour undersaturation in
757 primitive mid-ocean-ridge basalt and the volatile content of Earth's upper mantle. *Nature*
758 **419**, 451–5.
759 Sanchez S., Ahlberg P. E., Trinajstic K. M., Mirone A. and Tafforeau P. (2012) Three
760 Dimensional Synchrotron Virtual Paleohistology: A New Insight into the World of
761 Fossil Bone Microstructures. *Microsc. Microanal.* **18**, 1095–1105.
762 Sano Y. and Marty B. (1995) Origin of carbon in fumarolic gas from island arcs. *Chem. Geol.*
763 **119**, 265–274.
764 Schiano P., Provost A., Clocchiatti R., Faure F., Schiano P., Provost A., Clocchiatti R. and
765 Faurelt F. (2006) Transcrystalline Melt Migration and Earth's Mantle. *Science (80-.).*
766 **314**, 970–974.
767 Shcheka S. S., Wiedenbeck M., Frost D. J. and Keppler H. (2006) Carbon solubility in mantle
768 minerals. *Earth Planet. Sci. Lett.* **245**, 730–742.
769 Sherwood Lollar B., Ballentine C. J. and Onions R. K. (1997) The fate of mantle-derived
770 carbon in a continental sedimentary basin: Integration of relationships and stable isotope
771 signatures. *Geochim. Cosmochim. Acta* **61**, 2295–2307.
772 Shishkina T. a., Botcharnikov R. E., Holtz F., Almeev R. R. and Portnyagin M. V. (2010)
773 Solubility of H2O- and CO2-bearing fluids in tholeiitic basalts at pressures up to

500MPa. *Chem. Geol.* **277**, 115–125.

Sleep N. H., Zahnle K. J. and Neuhoff P. S. (2001) Initiation of clement surface conditions on the earliest Earth. *Proc. Nat. Acad. Sci.* **98**, 3666–3672.

Spakman W. (1990) Tomographic images on the upper mantle below Europe and the Mediterranean. *Ter. Nov.* **2**, 542–553.

Span R. and Wagner W. (1996) A New Equation of State for Carbon Dioxide Covering the Fluid Region from the Triple-Point Temperature to 1100 K at Pressures up to 800 MPa. *J. Phys. Chem.* **25**, 1509–1596.

Stephant A., Remusat L., Thomen A. and Robert F. (2014) Reduction of OH contamination in quantification of water contents using NanoSIMS imaging. *Chem. Geol.* **380**, 20–26.

Sterner S. M. and Pitzer K. S. (1994) An equation of state for carbon dioxide valid from zero to extreme pressures. *Contrib. to Mineral. Petrol.* **117**, 362–374.

Szabó C., Harangi S. and Csontos L. (1992) Review of Neogene and Quaternary volcanism of the Carpathian-Pannonian region. *Tectonophysics* **208**, 243–256.

Szabó C., Kovacs I., Dégi J., Kothay K., Torok K., Hidas K. K., Konya P., Berkesi M., Degi J., Kothay K., Torok K., Hidas K. K., Konya P. and Berkesi M. (2010) From maars to lava lakes: Ultramafic and granulite xenoliths associated with the alkaline basaltic volcanism of the Pannonian Basin. In *Mineralogica-petrographica field guide series* pp. 1–32.

Tašárová A., Afonso J. C., Bielik M., Götze H.-J. and Hók J. (2009) The lithospheric structure of the Western Carpathian–Pannonian Basin region based on the CELEBRATION 2000 seismic experiment and gravity modelling. *Tectonophysics* **475**, 454–469.

Wallace P. J. (2005) Volatiles in subduction zone magmas: concentrations and fluxes based on melt inclusion and volcanic gas data. *J. Volcanol. Geotherm. Res.* **140**, 217–240.

Wijbrans J., Németh K., Martin U. and Balogh K. (2007) 40Ar/39Ar geochronology of

799 Neogene phreatomagmatic volcanism in the western Pannonian Basin, Hungary. *J.*
800 *Volcanol. Geotherm. Res.* **164**, 193–204. Youxue Zhang and Zindler A. (1993)
801 Distribution and evolution of carbon and nitrogen in Earth. *Earth Planet. Sci. Lett.* **117**,
802 331–345.
803

Figures captions

Figure 1: Principles of synchrotron X-ray microtomography. a- Sample is placed into the beam in different angular positions; the transmitted beam is saved by the detector. b- All radiographs obtained are compiled and a 3D image is reconstructed mathematically. c- Each voxel of the 3D image is assigned to a grey level proportional to the local attenuation coefficient of the incident beam. d- Example of drilled peridotite sample.

Figure 2: Reconstructed X-ray tomography 3D image of the SZB51 sample (4 mm diameter). The dark grey phase is orthopyroxene, the medium-grey grey phase is olivine and the white is clinopyroxene. We can observe in black the grain boundaries, cracks and some trails of secondary fluid inclusions.

Figure 3: Density histograms of xenolith SZB51 (A, B) and xenolith FT12 (C, D) acquired by X-ray tomography. Left: full histograms. Right: deconvolved histogram with density peak assignment (B, D).

Figure 4: Example of phase density threshold defining for fluid vesicle segmentation of xenolith SZB51. Three cases of density threshold assigning were defined for each sample. The “Chosen fluid threshold” is considered the best estimated threshold. The minimum (“Min. fluid threshold”) and maximum (“Max. fluid threshold”) thresholds represent the upper and lower acceptable values near the best estimate. These provide a sense of the uncertainty associated with the user defined density threshold assigning.

Figure 5: NanoSIMS CO_2 and H_2O calibration curves (dashed curves) obtained with the tholeiitic glass standards (black dots) provided by CRPG, Nancy, France [standard description available in Shishkina et al. (2010)]. CO_2 and H_2O were normalized to SiO_2.

Figure 6: X-ray microtomography images illustrating the variety of textures and the different evidences of glass and fluid inclusions in mantle xenoliths. a - Protogranular texture. b- Equigranular mosaic texture. c- Equigranular tabular texture. d- Melt pocket with large vesicles (Vs), glass (Gl) and secondary crystallized minerals. e- A melt vein (glass + vesicles) and trails of secondary fluid inclusions (FI). Opx – orthopyroxene, Ol – olivine, Opx – orthopyroxene, SP- spinel, Gl – glass, Vs – vesicle.

Figure 7: 3D representation of the segmented volumes of glass (blue) and fluid (pink and black) obtained by X-ray tomography in xenolith SZB51 (4 mm diameter). This image clearly illustrates the crosscutting relationship between trails of fluid inclusions and glass+vesicles along grain boundaries. In this sample 5 Vol. % of the fluid phase is in fluid inclusions (black) and 95 Vol. % is in vesicles (pink) trapped in glass.

Figure 8: Example of melt pocket volume segmentation based on X-ray tomography. Pink, blue and brown phases refer to vesicles, glass and newly formed minerals, respectively.

Figure 9: a- Abundances of glass, fluid (FI + vesicles) and mineral assemblages for each studied xenoliths (Creon et al., this volume); b- AbundanceFluid inclusion abundances by host mineral in SZB51.

Figure 10: Glass and fluid volume correlation. Arrows indicate the crystal fractionation correction of the glass volume. Diamonds represent xenoliths with melt pockets + melt veins; circles represent xenoliths containing only melt veins. Black, dark-grey and light-grey symbols represent respectively SZB (Szentbékkálla), SZG (Szigliget) and FT (Füzes-tó) xenoliths.

Figure 11: Comparison between calculated densities based on EPMA chemical analyses (Dixon et al., 1995) and measured densities by X-ray micro-CT for olivine, orthopyroxene, clinipyroxene and glass. The shaded areas correspond to density range for melt of basalt, andesite and trachyte (Richet et al. 2000 and references therein)

Figure 12: A- Correlation between density determination methods (Raman spectroscopy vs. microthermometry); B- Histogram of FI density for locations of the studied xenoliths (SZB - Szentbékkálla, SZG - Szigliget & FT - Füzes-tó)

Figure 13: CO_2 saturation curves calculated with rhyolite-MELTS (Gualda et al., 2012; Ghiorso and Gualda, 2015) at 1000 °C using glass compositions obtained by EMPA and H_2O contents obtained by Nano-SIMS measurements. Saturation pressure estimates of the melt prior to quenching are defined by the intercept of the CO_2 contents in glass (NanoSIMS data) and the CO_2 saturation curves (grey lines). Black diamonds: SZB xenoliths), dark-grey diamonds: SZG xenoliths) and light-grey diamonds: FT xenoliths)

Figure 14: H_2O vs. CO_2 for glass trapped as vein or melt pockets in SZB (Szentbekkalla); SZG (Szigliget) and FT (Füzes-tó) mantle xenoliths. For comparison melt inclusions from arc

basalts are shown (Grey fields, Modified from Wallace, 2005). Literature data are shown for Cerro Negro (Roggensack et al., 1997), Fuego (Fg; Roggensack 2001), Guatemalan volcanoes behind the volcanic front (Guat BVF; Walker et al. 2003), the Trans-Mexican Volcanic Belt (Luhr, 2001; Cervantes and Wallace, 2003), Stromboli (Metrich et al., 2001) and Cayuse Crater, a cinder cone with OIB-like trace element composition from the Oregon Cascades (Cas OIB; M. Rowe, unpublished data). For Cerro Negro, only inclusions from the 1992 explosive eruption are plotted. For comparison primary CO_2 contents of N-MORB (Marty and Tolstikhin, 1998), E-MORB (Hekinian et al., 2000), Kilauea basalt (Gerlach et al., 2002) and popping-rock (Graham and Sarda, 1991) are shown. Also shown is the CO_2 content of basaltic magma from Reunion based on rare high-pressure melt inclusions (Bureau et al., 1999). SZB, Szentbékkálla; SZG, Szigliget; FT, Füzes-tó; Fuego; Guat (BVF), Guatemalan volcanoes behind the volcanic front; Mexico, the Trans-volcanic Belt; Stromb., Stromboli; Cas OIB, Cayuse Crater from the Oregon Cascades.

Figure 15: H_2O vs. CO_2 diagram illustrating the NanoSIMS data from peridotite hosted glass, and the reconstructed CO_2 contents of the melt+fluid system. For comparison, subducted sediments from Plank and Langmuir (1998), altered MORB from Staudigel et al. (1989), N-MORB from Marty and Tolstikhin (1998), E-MORB from Hekinian et al. (2000) are shown. Green area corresponds to the range of compositions of the subducting crust. Pink area corresponds to plausible compositions for magmas produced from incongruent melting of the subducted crust. Blue area corresponds to melts relatively depleted in volatiles issued from slab melting and modified by subsequent volatile depletion, such as the assimilation of volatile poor material and/or some physical fractionation during magma decompression.

Figure 1

Click here to download high resolution image

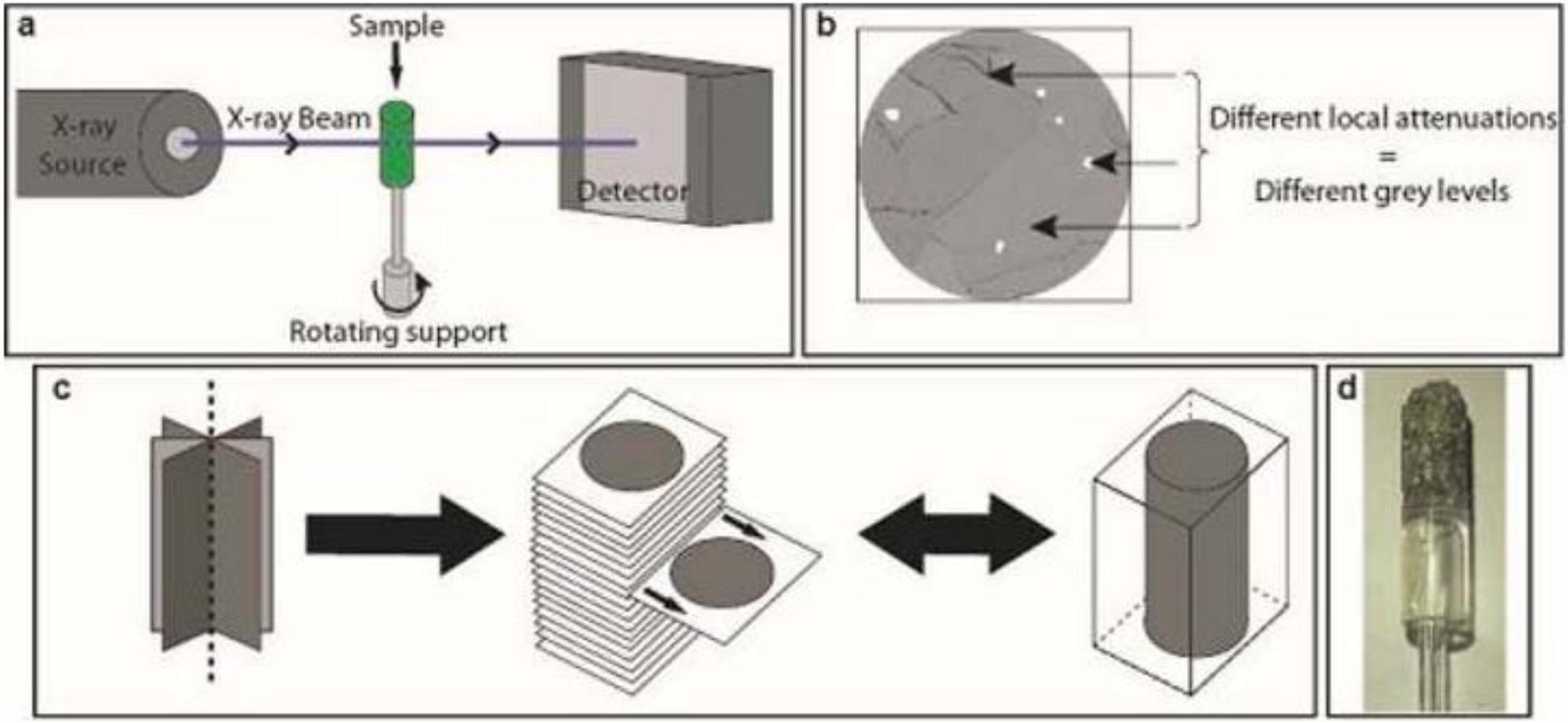

Figure 2

Click here to download high resolution image

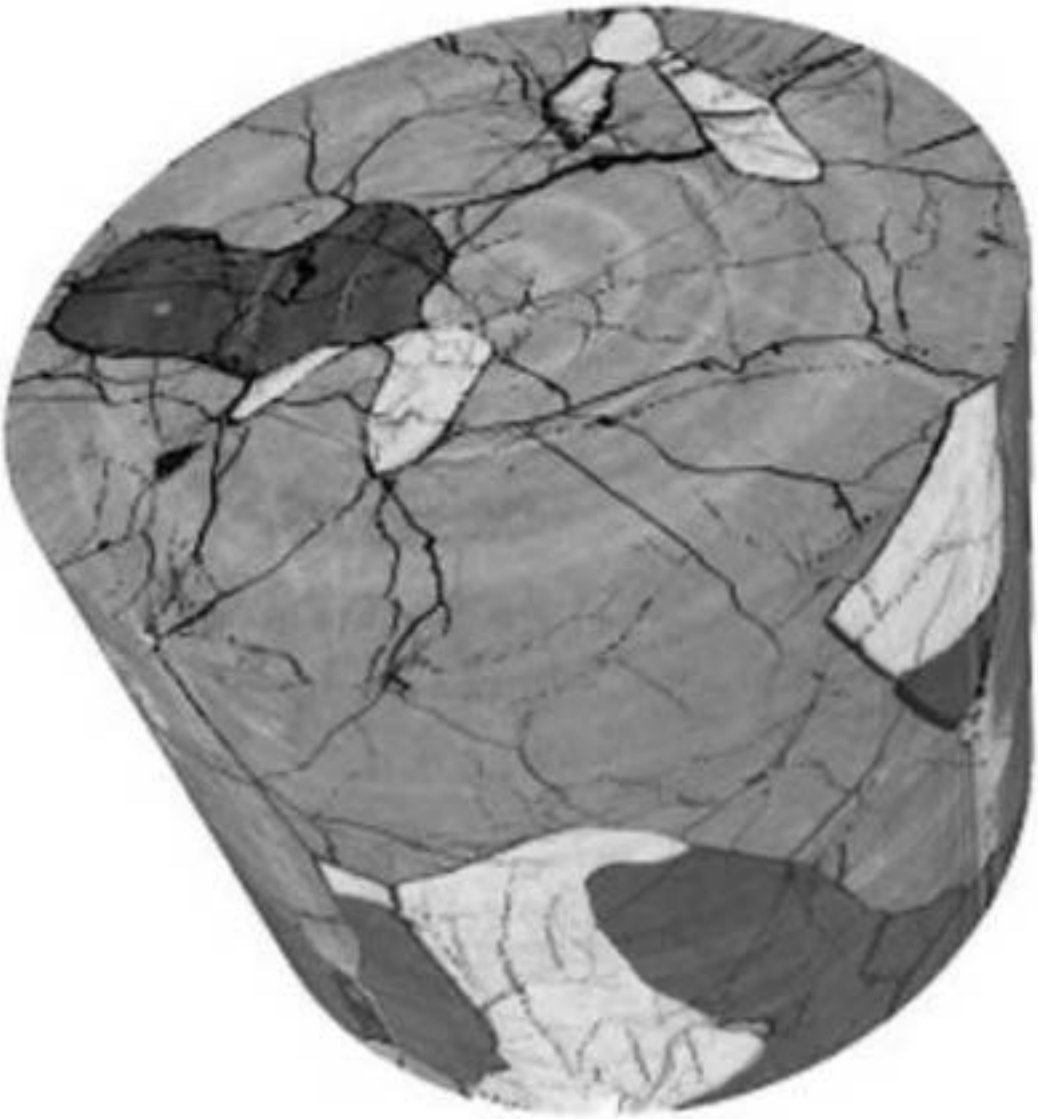

Figure 3

Click here to download high resolution image

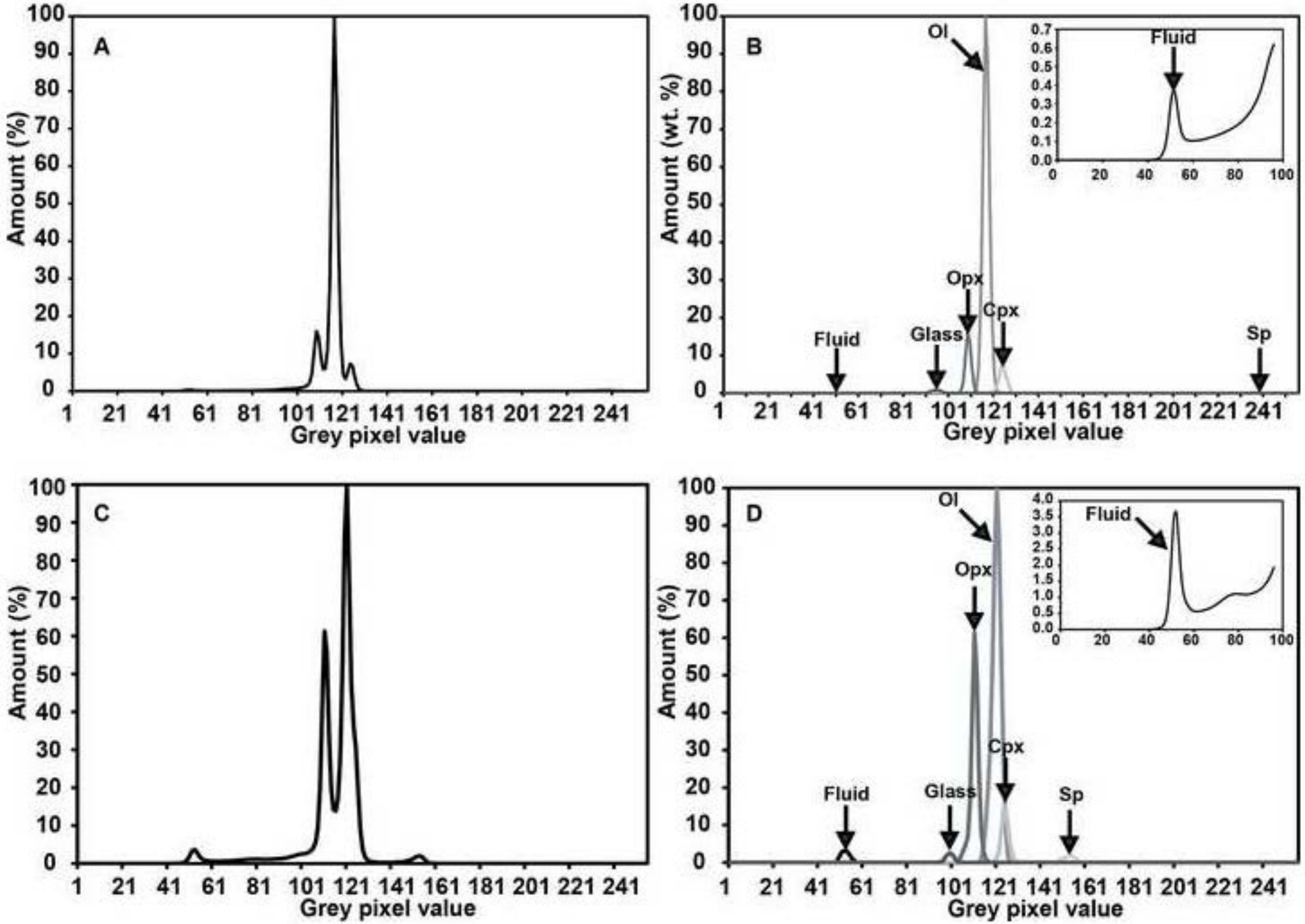

Figure 4

Click here to download high resolution image

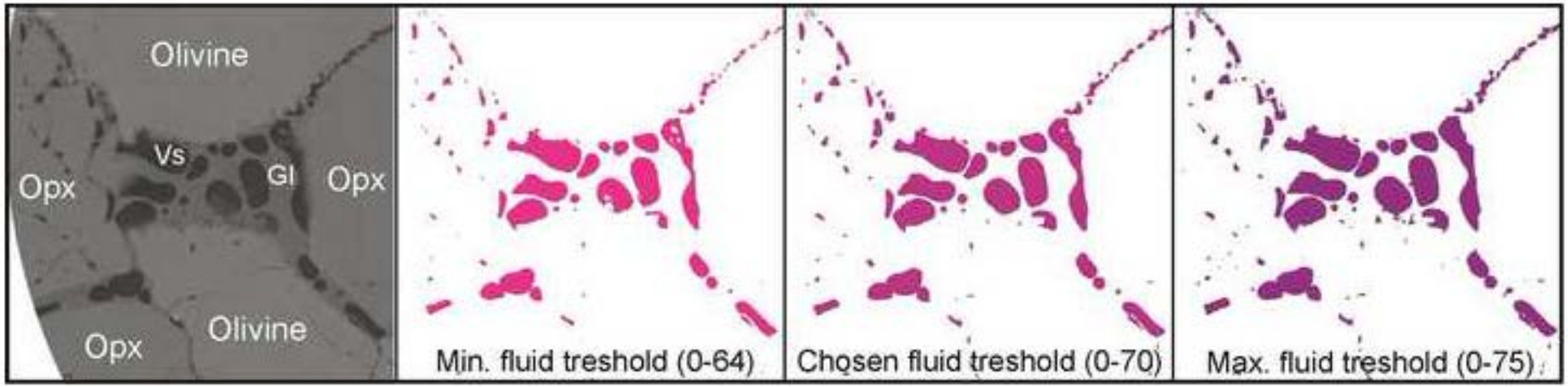

Figure 5

Click here to download high resolution image

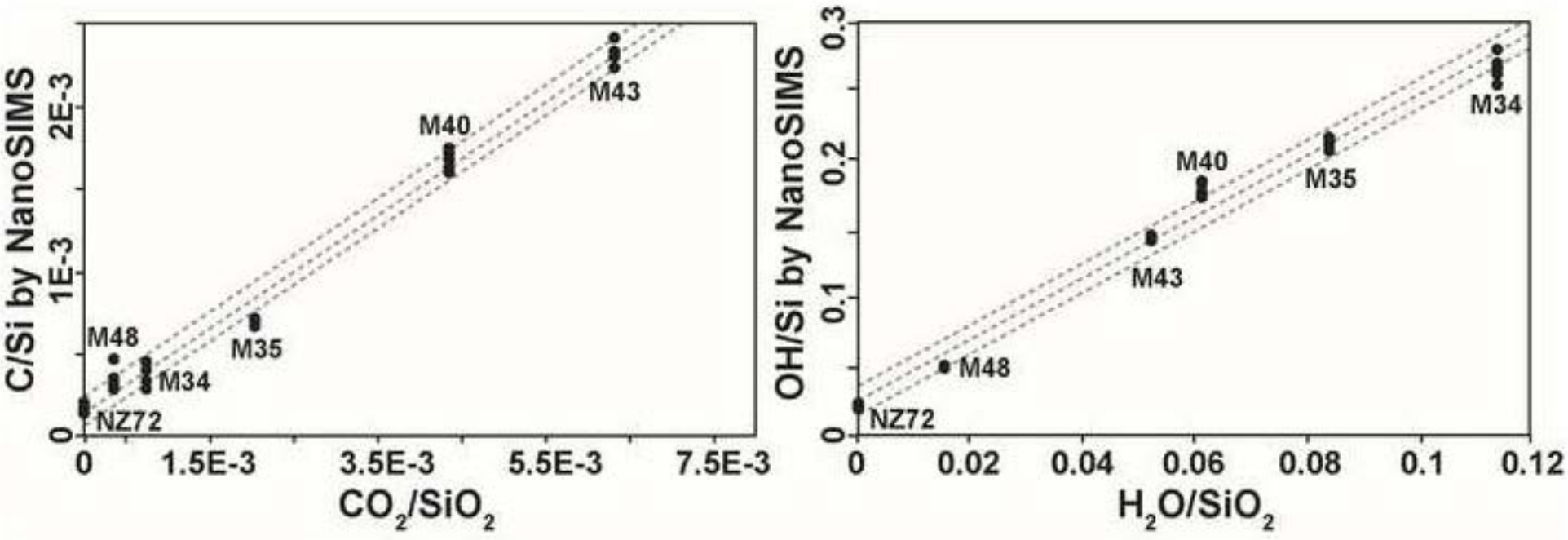

Figure 6

Click here to download high resolution image

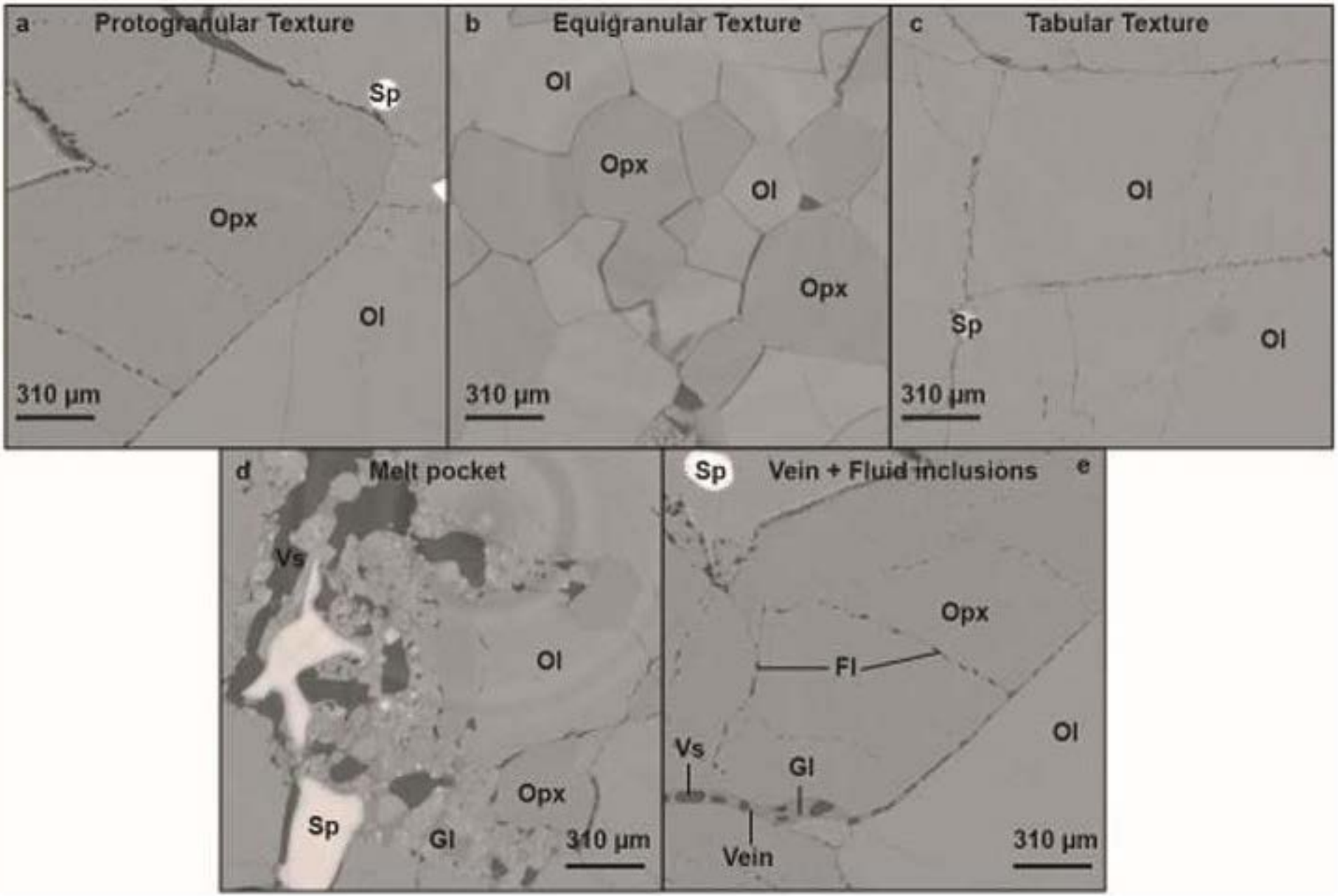

Figure 7

Click here to download high resolution image

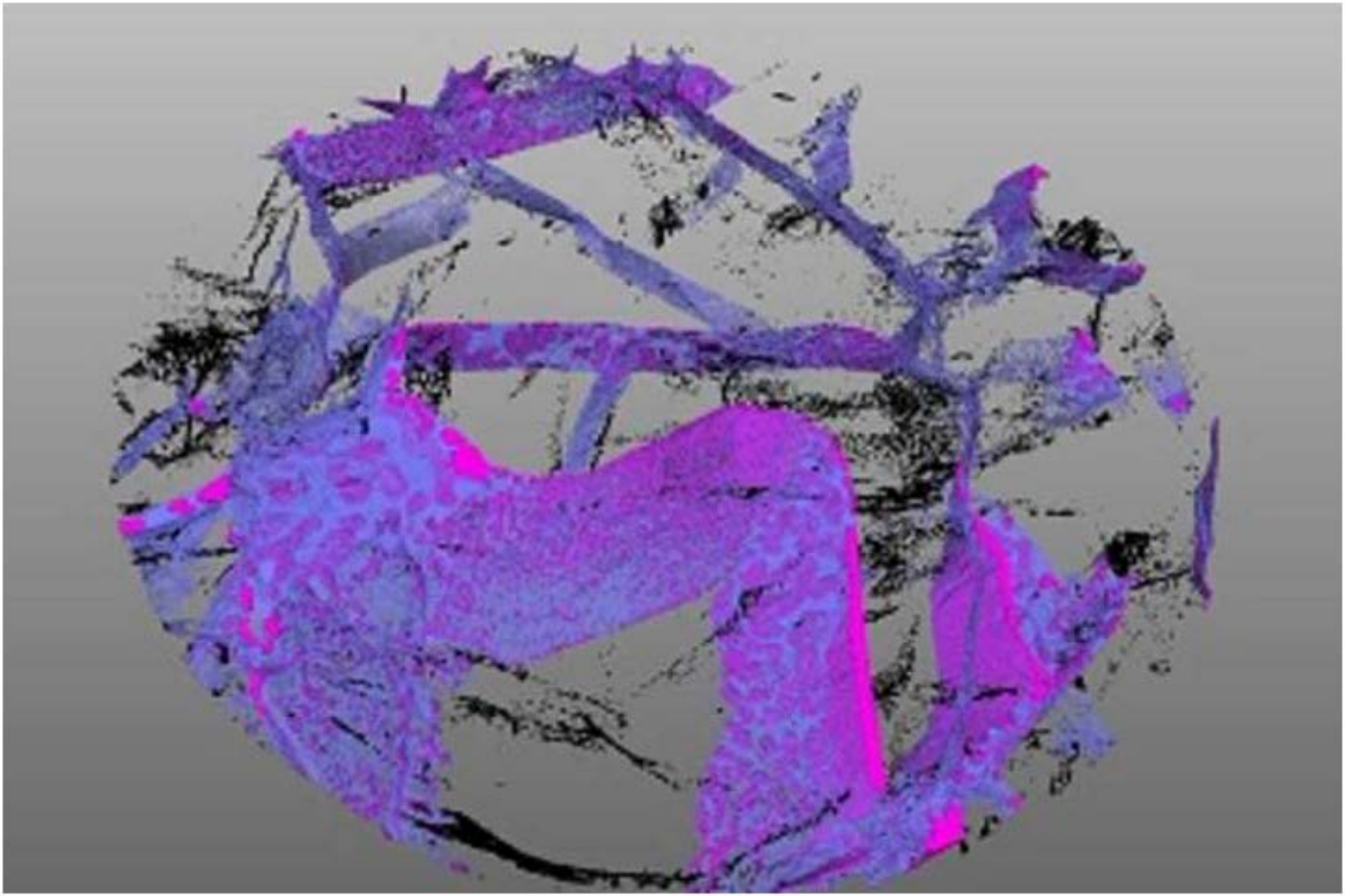

Figure 8

Click here to download high resolution image

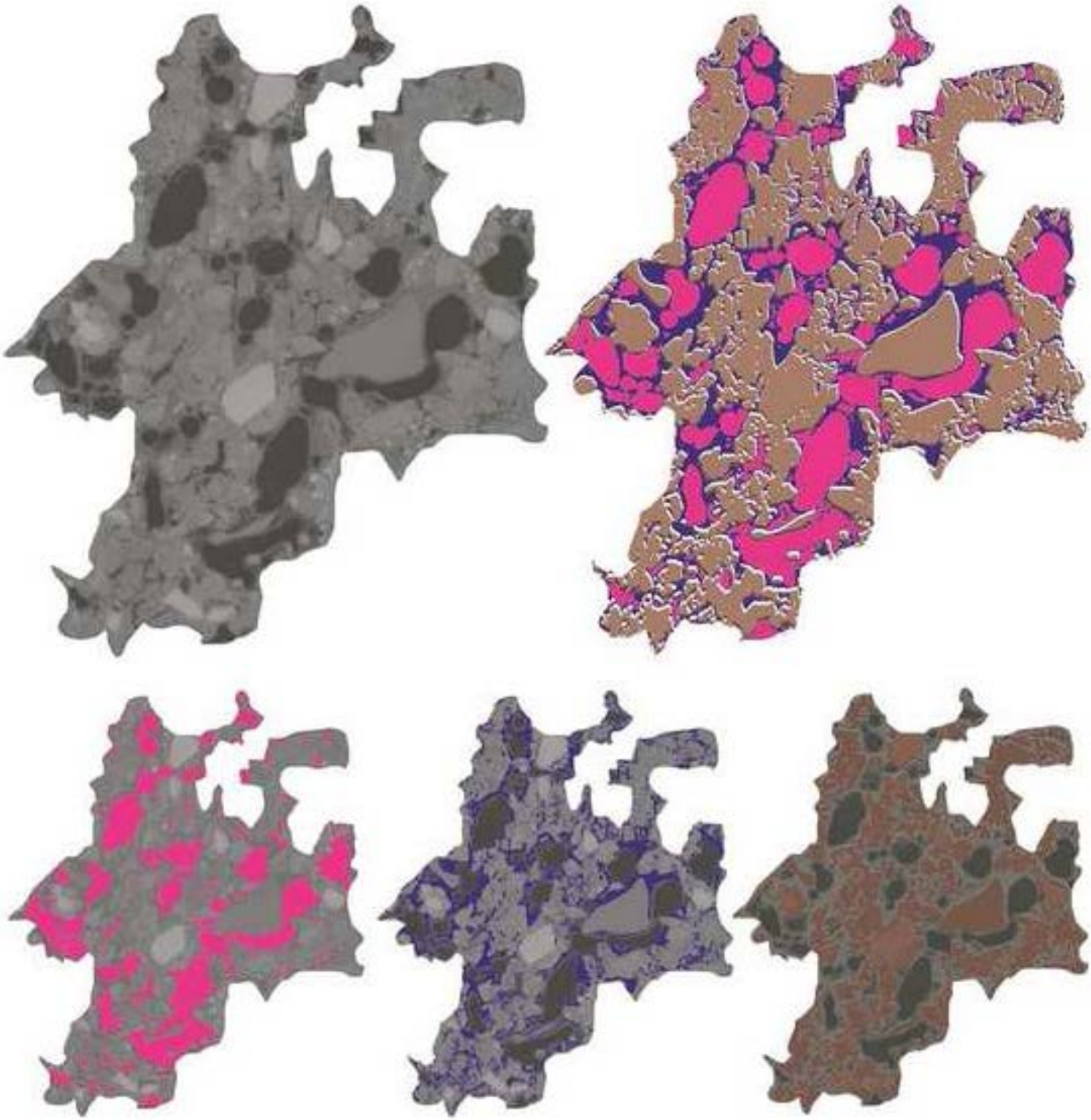

Figure 9

Click here to download high resolution image

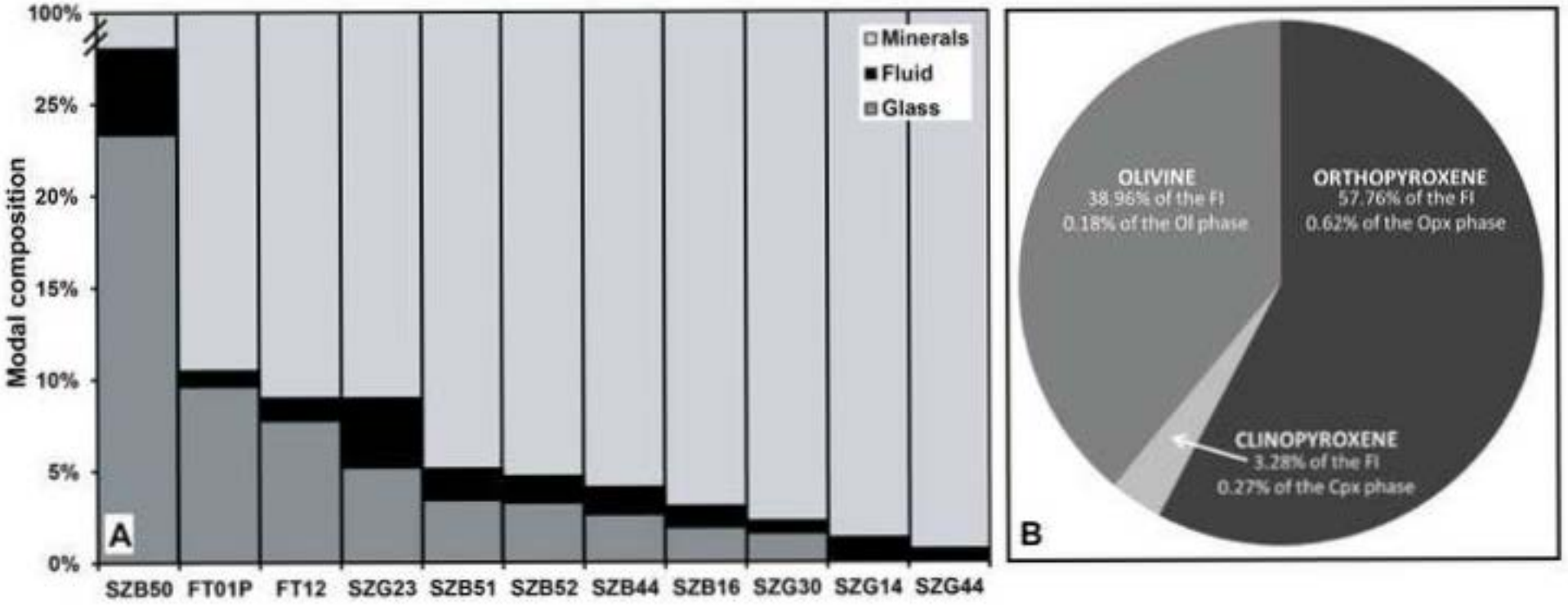

Figure 10

Click here to download high resolution image

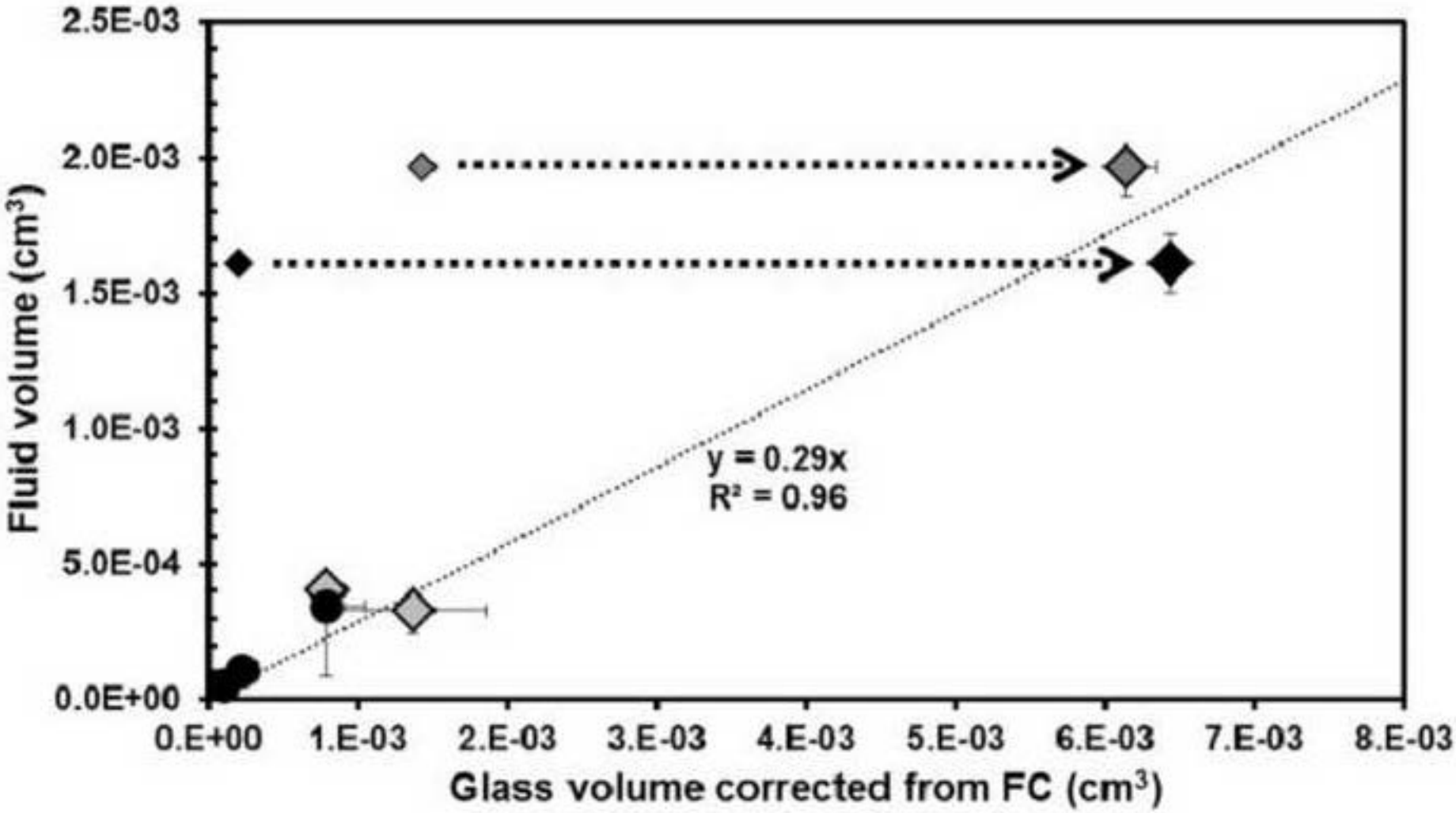

Figure 11

Click here to download high resolution image

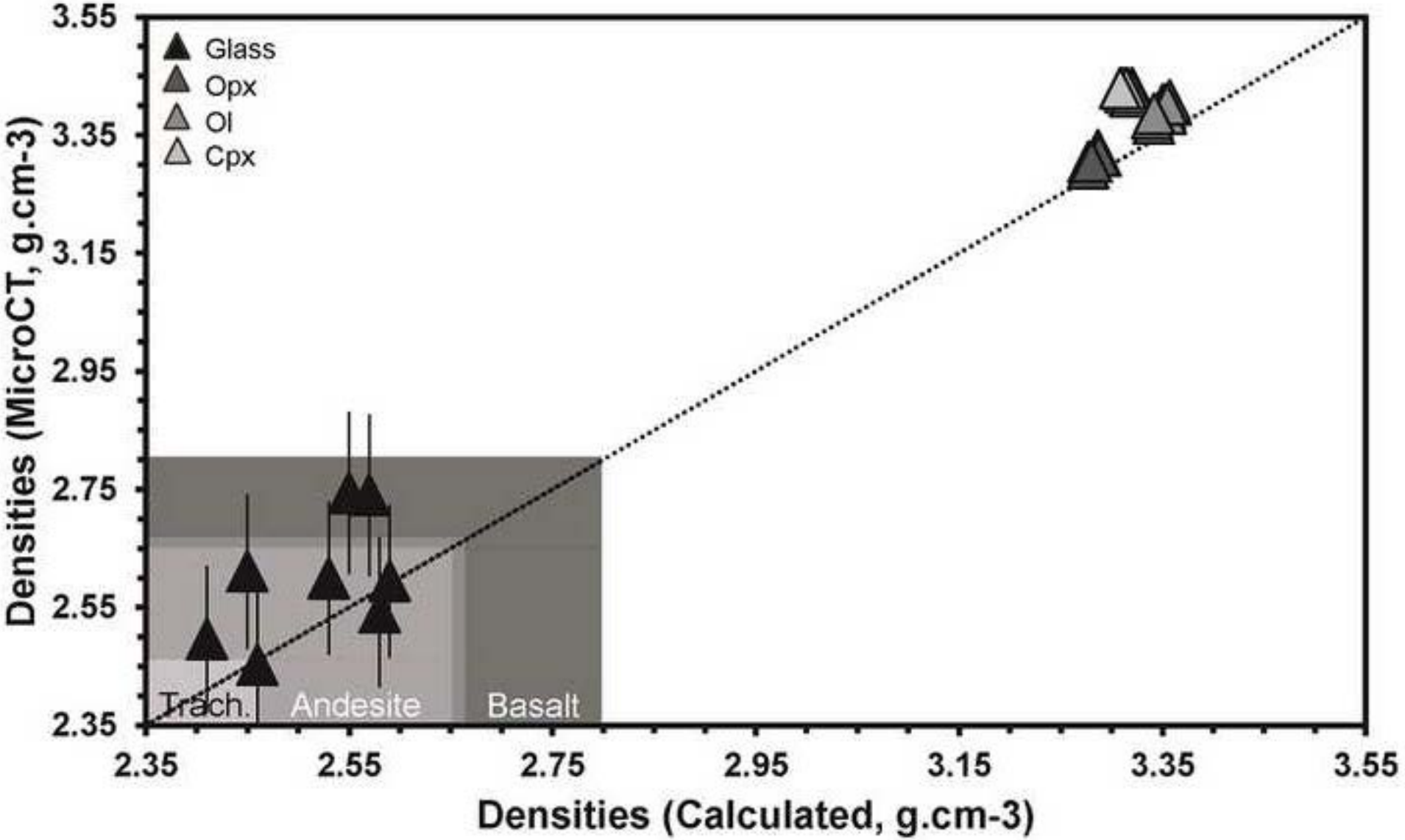

Figure 12

Click here to download high resolution image

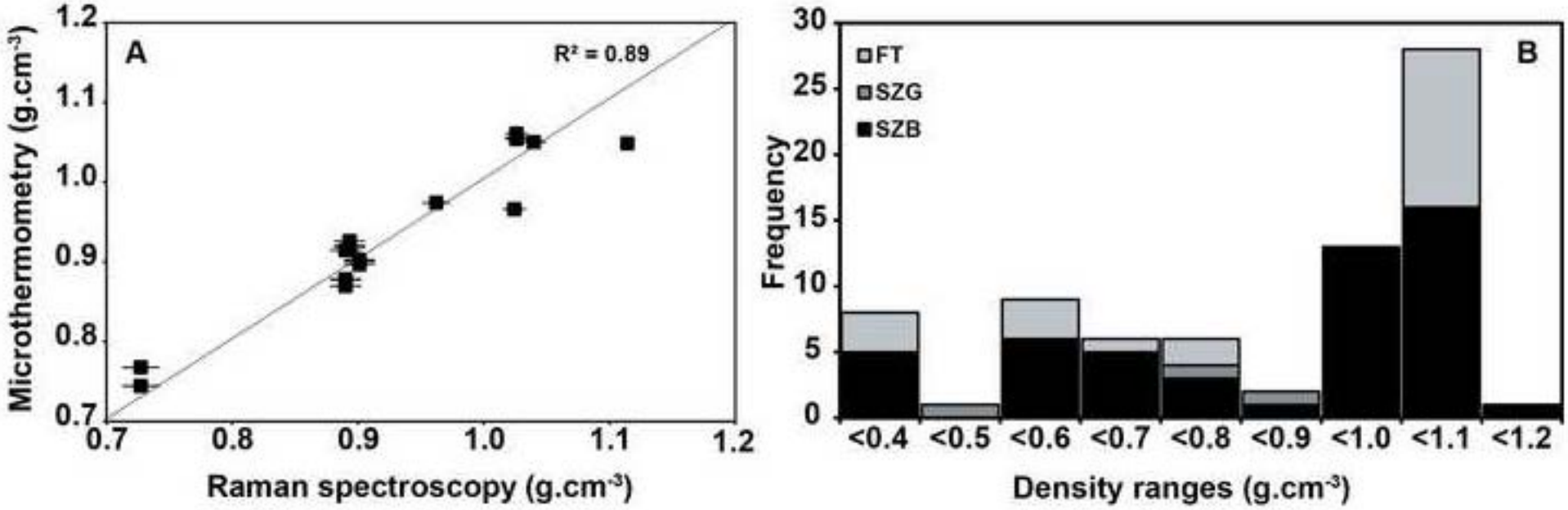

Figure 13

Click here to download high resolution image

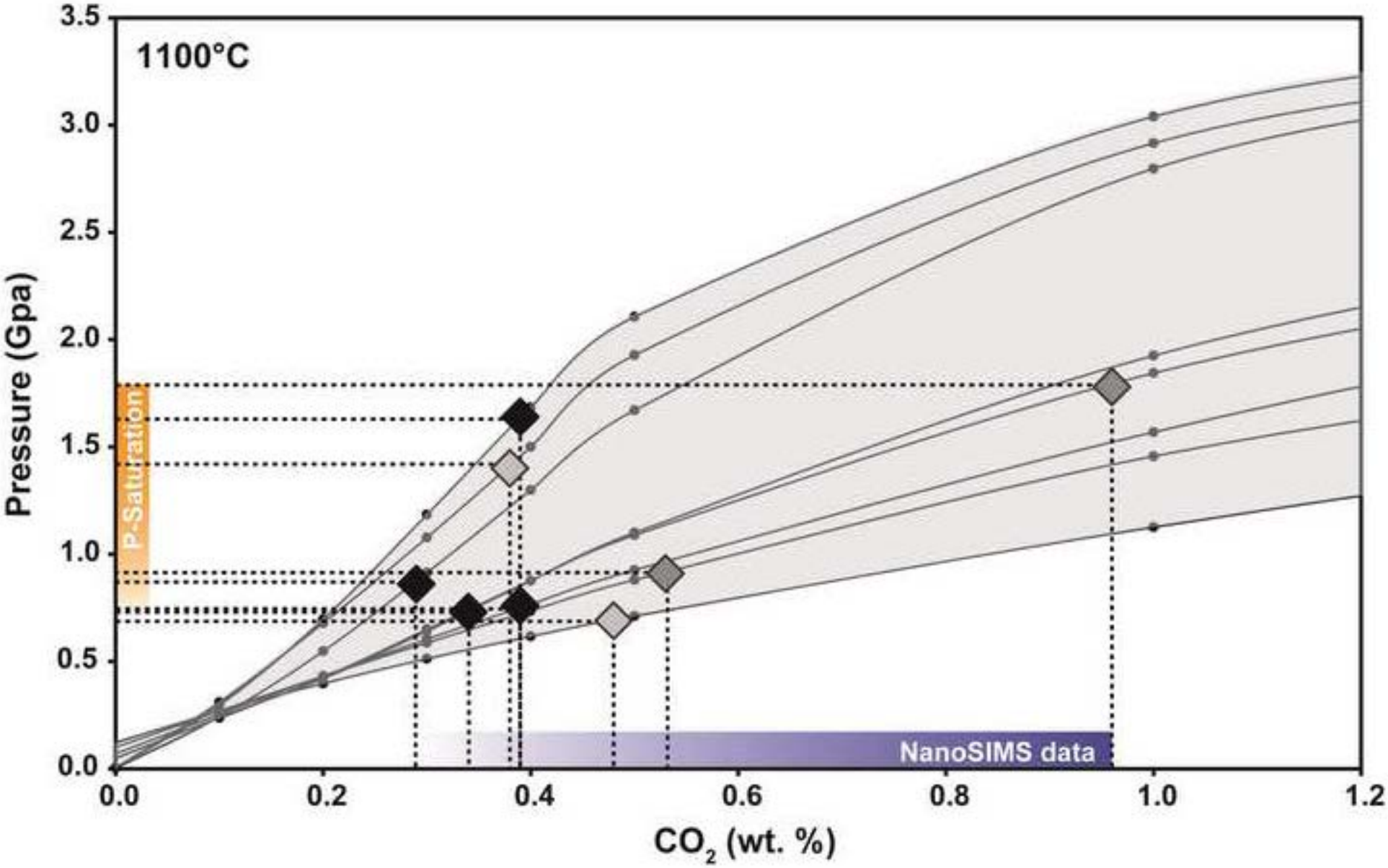

Figure 14

Click here to download high resolution image

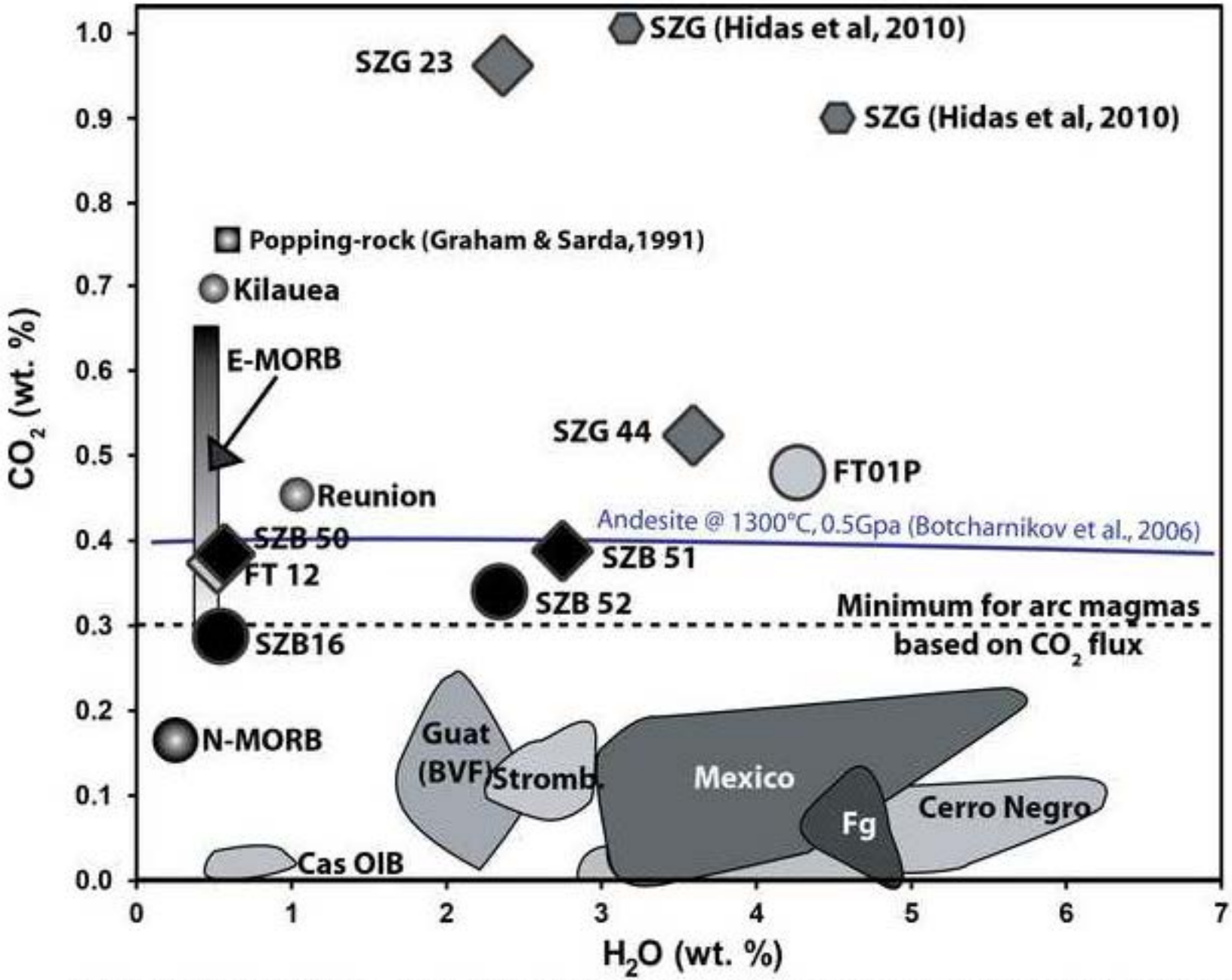

SZB, Szentbékkálla; SZG, Szigliget; FT, Füzes-Tó; Fg, Fuego; Guat (BVF),Guatemalan volcanoes behind the volcanic front, Mexico, the Trans-Mexican Volcanic Belt; Stromb., Stromboli; Cas OIB, Cayuse Crater from the Oregon Cascades

Figure 15

Click here to download high resolution image

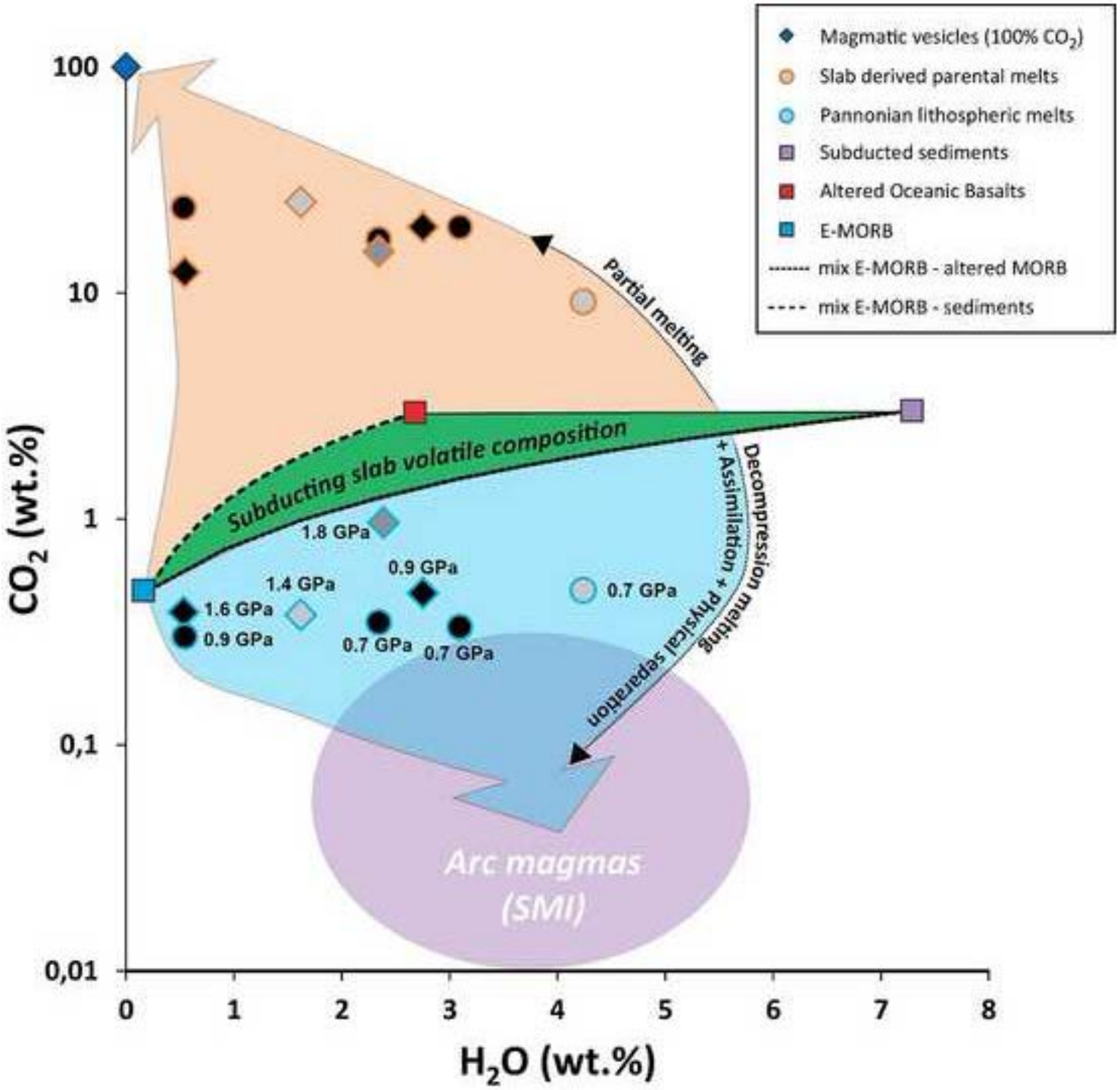

Table 1

Click here to download Table: Table 1.doc

							Vol. (cm^3)	Glass volume (cm^3)			Fluid volume (cm^3)			Density (g/cm^3)			Mass (g)				
Sample	**MP**	**SiO_2**	**H_2O**	**Error (1σ)**	**CO_2**	**Error (1σ)**	**Minerals**	**Best estimate**	**Min (%)**	**Max (%)**	**Best estimate**	**Min (%)**	**Max (%)**	**Glass**	**Vesicles**	**FI (Max)**	**Glass**	**CO_2 (vesicle)**	**CO_2 (dissolved)**	**CO_2/glass (wt. %)**	**CO_2/π (ppm)**
SZB16	no	56.6	0.54	0.26	0.29	0.14	4.6E-03	9.1E-05	3.7E+01	1.3E+01	5.5E-05	1.5E+01	3.3E+01	2.599	1.022	0.573	2.4E-04	5.6E-05	6.8E-07	24.1	3723
SZB50	no	55.4	0.59	0.26	0.39	0.14	3.1E-02	6.4E-03	6.6E+00	6.4E+00	1.6E-03	1.3E+00	1.4E+01	2.740	1.295	0.617	1.8E-02	2.1E-03	6.8E-05	12.2	21287
SZB51-v	no	61.9	3.1	0.26	0.33	0.16	6.0E-03	2.1E-04	1.4E+01	2.6E-04	1.1E-04	3.2E+01	2.0E+01	2.496	0.970	1.024	5.3E-04	1.0E-04	2.1E-06	19.9	5409
SZB51-MP	yes	56.6	2.76	0.28	0.46	0.15															
SZB51-Av	yes	59.6	2.95	0.28	0.39	0.16															
SZB52	no	57.9	2.35	0.26	0.34	0.15	2.3E-02	7.8E-04	1.3E+01	1.0E-03	3.4E-04	5.8E+00	3.4E+01	2.452	0.953	1.114	1.9E-03	3.3E-04	6.5E-06	17.4	4422
SZG23	yes	56.3	2.38	0.26	0.96	0.20	3.5E-02	6.1E-03	2.3E+00	1.6E-03	2.0E-03	3.2E+00	1.3E+01	2.744	1.330	0.703	1.7E-02	2.6E-03	1.6E-04	16.5	24383
SZG44	yes	51.7	3.45	0.24	0.53	0.14	nd		0.0E+00	0.0E+00	1.3E-04	nd	nd	0.000	1.045	0.824	nd	1.4E-04	nd	nd	nd
FT12	yes	54.8	0.55	0.26	0.38	0.14	3.1E-02	7.8E-04	4.2E+00	9.7E-04	4.0E-04	1.0E+01	1.5E+01	2.542	1.228	0.661	2.0E-03	5.0E-04	7.5E-06	25.4	4946
FT01P	no	57.8	4.25	0.27	0.48	0.16	3.6E-02	1.4E-03	9.3E+00	1.7E-03	3.3E-04	4.9E+01	3.9E+01	2.611	0.930	1.057	3.6E-03	3.0E-04	1.7E-05	9.0	2727

Table 1: Summary of petrographic observations, chemical compositions and phase volumes, densities and masses. V – vein; MP – melt pocket; Av – average composition; Vol. – volume; Min & Max – Relative determined errors for each best estimate; vs - vesicle; FI – fluid inclusion; gl – glass; π - peridotite